https://doi.org/10.5194/se-2021-151
Preprint. Discussion started: 4 January 2022

Solid Earth
Discussions
Open Access
EGU

Regional mantle viscosity constraints for North America reveal upper mantle strength differences across the continent.

Osei Tutu, Anthony and Harig, Christopher
Department of Geosciences, University of Arizona, Tucson
Correspondence: Osei Tutu, Anthony (oseitutu@arizona.edu)

Abstract. We present regional constraints of mantle viscosity for North America using a local Bayesian joint inversion of mantle flow and glacial isostatic adjustment (GIA) models. Our localized mantle flow model uses new local geoid kernels created via spatio-spectral localization using Slepain basis functions, convolved with seismically derived mantle density to calculate and constrain against the regional free-air gravity field. The joint inversion with GIA uses two deglaciation of ice sheet models (GLAC1D-NA and ICE-6G-NA) and surface relative sea level data. We solve for the local 1D mantle viscosity structure for the entire North America (NA) region, the eastern region including Hudson Bay, and the western region of North America extending into the Pacific plate.

Our results for the entire NA region show one order of magnitude viscosity jump at the 670 km boundary using a high seismic density scaling parameter (e.g., $\delta ln\rho/\delta lnv_S = 0.3$). Seismic scaling parameter demonstrates significant influence on the resulting viscosity profile. However, when the NA region is further localized into eastern and western parts, the scaling factor becomes much less important for dictating the resulting upper mantle viscosity characteristics. Rather the respective local mantle density heterogeneities provide the dominate control on the upper mantle viscosity. We infer local 1D viscosity profiles that reflect the respective tectonic settings of each region's upper mantle, including a weak and shallow asthenosphere layer in the west, and deep sharp viscosity jumps in the eastern transition zone, below the suggested/proposed depth range of the eastern continental root.

1 Introduction

The broad tectonic regime of the North America (NA) continent is characterized by thick cratonic lithosphere in the east, and thin lithosphere with shallow hot mantle material in the west (Hyndman, 2017). Observed surface vertical motion centered in the Hudson Bay area (Tamisiea et al., 2007; Kreemer et al., 2018) have been linked to the loading and unloading of the Laurentide ice sheet during the last 21,000 years (Dyke, 1987; Wu and Peltier, 1982). The response rates of the Earth's mantle and lithosphere to surface mass change (Haskell, 1935) is modulated through elastic and viscous deformation at different spatiotemporal scales. Using glacial isostatic adjustment (GIA) techniques a number of studies (e.g., Mitrovica and Forte,

https://doi.org/10.5194/se-2021-151
Preprint. Discussion started: 4 January 2022

1997; Wu and Peltier, 1982; Tamisiea et al., 2007; Lambeck et al., 1998; Wu and Peltier, 1983; Tushingham and Peltier, 1991; Mitrovica et al., 1994; Mitrovica, 1996; Forte and Mitrovica, 1996; Mitrovica and Peltier, 1995) have inferred a range viscosity values of the mantle based on either 1D or 3D forward and inverse modeling.

Regional studies of the Hudson Bay low gravity anomaly (e.g., Simons and Hager, 1997; Pari and Peltier, 2000) suggest a possible signal overprint from postglacial and mantle convection effects. Simons and Hager (1997) analyzed fee-air gravity data and argued that about half of the observed crustal depressions is due to the fingerprints of the Laurentide ice sheet load, while the remaining signal is the influence dynamic topography, coming from the downwelling of the ancient Kula–Farallon slab (Forte et al., 2010). Similar synthesis of postglacial, seismic data and free-air gravity data by Pari and Peltier (1996, 2000) studied the dynamic and compositional characteristics of the upper mantle and craton, and showed that just about 10% of the observed low gravity anomaly underlying the footprint of the now disappeared Laurentide ice sheet is due to deglaciation.

Recent inferences of mantle viscosity using mantle flow and GIA modeling of the long-wavelength gravity field (Reusen et al., 2020), found that about 60% of the low static gravity anomaly maybe due to dynamic topography. The coupling of the postglacial signal, thermal/density and rheological dynamics in the presence of thick continental root, and a downward pull of the Farallon slab reveal a complex mantle structure generating the Hudson Bay gravity anomaly. Likewise, the western part of NA continental area is also shaped by GIA effects of the Laurentide and Cascadia ice sheets, as well as tectonic overprints coming from the dynamics of the Cascadia and Aleutian-Alaska subduction systems. GIA studies of the Pacific west (James et al., 2009b, a; Roy and Peltier, 2015; Yousefi et al., 2021, 2018) show an even more complex region with a wide range of crust and mantle temperatures, seismic activities, and postglacial dynamics. Yousefi et al. (2018) explored these in GIA inversion studies to constraints the regional 1D Earth model testing different RSL curves and correcting for tectonic activities for viscosity inversion.

Mitrovica and Forte (1997) combined GIA and large-scale mantle flow calculations in a joint inversion to constrain viscosity depth-variations for more than three layers within the mantle. Their hybrid inversion technique (Mitrovica and Forte, 1997, 2004) showed considerable potential to address some of the differences that exist between mantle viscosity values using only postglacial rebound data (Cianetti et al., 2002; Lau et al., 2016) or mantle flow modeling (Steinberger and Calderwood, 2006), especially in the transition zone and the mid-mantle.

In this paper, we adopt a new joint inversion analysis for regional viscosity inferences to study local mantle rheology of the North America (NA) continental area. We infer a series of absolute and relative viscosity values in the upper mantle,, by varying model parametrization and data constraint. We explore the dynamic effect of density/thermal, rheological and postglacial rebound in the Hudson Bay region (Simons and Hager, 1997) and western NA region (Yousefi et al., 2018). We use *local* geoid sensitivity kernels (Fig. 1) in a mantle flow modeling scheme with GIA calculations to study *local* 1D viscosity structure considering more than 3 layers of the mantle and different seismic density scalings for the continent wide. We further

https://doi.org/10.5194/se-2021-151
Preprint. Discussion started: 4 January 2022

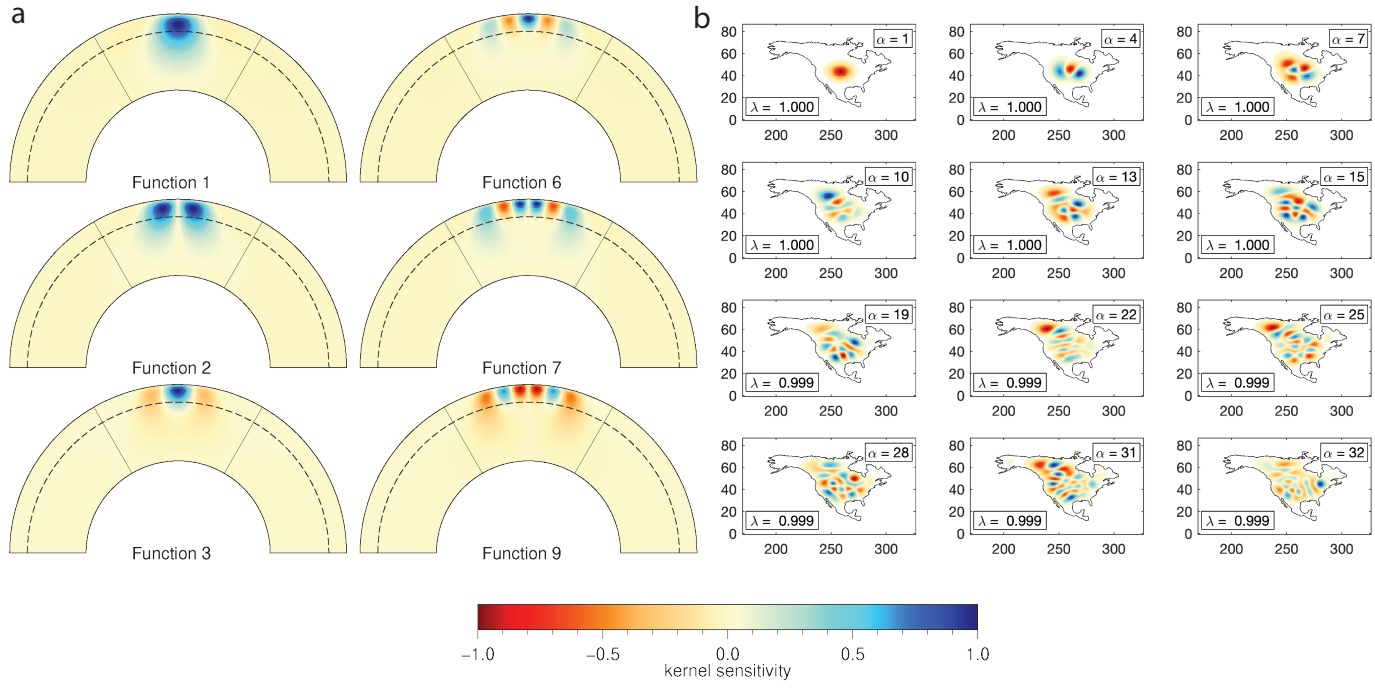

Figure 1. Local sensitivity dynamic geoid kernels with an isoviscous mantle. a) Shown is a cross-section along 0° and 180° in the northern hemisphere from the surface to the core mantle boundary. The kernels have azimuthal dependence and as such will have different manifestations at different azimuths. The kernels are localized to a 30° spherical cap, denoted by black lines connecting the surface to the core mantle boundary and the dashed lines show the 670 km depth. The bandwidth of the basis is $L = 15$. Functions are ranked by concentration within the region, and shown are functions 1, 2, 3, 6, 7, and 9. Here the kernels are normalized by their maximum absolute value. b) North America continental region showing plots of synthesized concentrated Slepian eigenfunctions. α indicates the eigenfunction number and rank while the eigenvalue concentration factors are labeled as λ within the coastlines. Similar plots showing our continent-wide region with outline R are given in appendix Figure 1A.

2 Methods

2.1 Slepain basis function and local geoid kernels

We develop local geoid sensitivity kernels using a Slepian function spectral localization technique (Wieczorek and Simons, 2005). Spatio-spectral localization techniques such as radial basis functions, wavelets (Schmidt et al., 2007) or point masses (Baur and Sneeuw, 2011) are a common way to analyze global potential fields (e.g., gravity or magnetic fields) in a local region on a sphere. A common drawback among some localization techniques is the loss of orthogonality of the basis functions

https://doi.org/10.5194/se-2021-151
Preprint. Discussion started: 4 January 2022

over the patial sphere. Regularization techniques can be applied to mitigate the loss of orthogonality, but often at increased computational cost and difficulty. Slepian basis functions have the main advantage that they are orthogonal on both the whole sphere and partial sphere, as well as often forming a sparse basis set (Wieczorek and Simons, 2005; Simons et al., 2006). Spatio-spectral localization via Slepian functions has been used in a variety of applications such as determining the mass balance of ice sheets using GRACE gravimetry data (Harig and Simons, 2012, 2015, 2016; Bevis et al., 2019), localizing and deriving earthquake gravitational signals from GRACE gravimetry (e.g. Han and Simons, 2008), mapping the South Polar magnetic field of Mars (A. Plattner, 2015), etc.

Slepian basis functions constitute a linear combination of spherical harmonic functions on the sphere (Ω), determined by an optimization within a local region of interest R (Wieczorek and Simons, 2005; Simons, 2009). We form Slepian functions for our study region R by integrating the products of the spherical harmonics Y_{lm} as

$$\int_R Y_{lm} Y_{l'm'} d\Omega = D_{lm,l'm'}. \tag{1}$$

Here, l and m are the spherical harmonic degree and order, respectively. The 'localization kernel' $\mathbf{D}$ is then decomposed in an eigenvalue equation,

$$\sum_{l'=0}^{L} \sum_{m'=-l'}^{l'} D_{lm,l'm'} g_{l'm'} = \lambda g_{lm}, \tag{2}$$

where the Slepian basis functions g_{lm} are the eigenfunctions of the localization problem and the eigenvalues $0 \leq \lambda \leq 1$ represent the degree of concentration of each function within the region R (Simons et al., 2006). The functions can easily be created for arbitrary regions such as continental North America (Fig. 1b and see also Figure A1) and the subset of well-concentrated functions (with $\lambda \geq 0.5$) form a convenient basis for local signal analysis.

We combine the Slepian basis functions from our localization procedure with non-linear gravitational Green's functions known as geoid kernels $\mathcal{G}^l(r, \eta(r))$ representing the dynamic contribution of the Earth's mantle to the anomalous geoid at the surface for a given viscosity structure η (Richards and Hager, 1984; Hager et al., 1985; Hager and Clayton, 1989; Davies and Richards, 1992). The global dynamic geoid anomaly is calculated as

$$\delta \mathcal{V}_{lm}(S) = \frac{4\pi G S}{2l+1} \int_c^S \mathcal{G}^l(r, \eta(r)) \delta \rho_{lm}(r) dr, \tag{3}$$

where G is the gravitational constant and $\delta\rho$ is density anomaly. r denotes the mantle radius between the surface S and the core mantle boundary c. The corresponding free-air gravity field is given as $F_l^m = g_o(l-1)/r_e * (\delta V_{lm})$. r_e and g_o are the radius of Earth's outer surface (i.e., 6371 km) and corresponding gravitational acceleration value respectively. We employ the Preliminary Reference Earth Model (PREM) (Dziewonski and Anderson, 1981) with prescribed mantle interfaces in calculating the geoid kernels for our estimation procedure (Fig. 2a) depicted by Vioronoi nuclie (green squares) at 80, 220, 410 and 670 km

https://doi.org/10.5194/se-2021-151
Preprint. Discussion started: 4 January 2022


Solid Earth Discussions

depths.

Our study uses three regions of interest — the broader North America region, western NA and Pacific, and the eastern cratonic region of NA — outlined in Fig. 2b–d. The traditional geoid kernels described in Equation 3 have consistent energy globally since spherical harmonics spread their energy globally. By instead expanding a bandlimited version of the geopotential (up to degree L) into Slepian functions, we can express the potential localized at the surface as

$$\mathcal{V}(\mathbf{r}) = \sum_{\alpha=1}^{(L+1)^2} \mathcal{V}_\alpha g_\alpha(\mathbf{r}), \tag{4a}$$

$$\mathcal{V}_\alpha(S) = \frac{4\pi G S}{2l+1} \int_c^S \mathcal{G}_\alpha(\mathbf{r}) \rho_{lm}(r) dr, \tag{4b}$$

$$\mathcal{G}_\alpha(r) = \sum_{\alpha=1}^{(L+1)^2} g_{\alpha,lm} \mathcal{G}_{lm}(r). \tag{4c}$$

Using a set of Slepian functions representing a polar cap (e.g., 30°) we transform the global kernels into *localized* versions in Fig. 1. Here, the now 3D geoid kernels localize their sensitivity within the region of interest and represent the sensitivity of a loading density to the geoid, within a *volume* of the mantle. Each function now includes power at a blend of degrees up to the bandlimit, and the functions are discriminated within the set by their amount of concentration in the region of interest represented in the eigenvalue λ.

We use seismic tomography model from French and Romanowicz (2015) for our regional mantle flow analysis to estimate the local gravity signal based on our local geoid kernels. We do not take into account the lateral variations in crustal thickness and set the top 150 km of the seismic derived density to uniform density. By inverting for the local relative viscosity structure using the local gravity kernels and jointly inverting with GIA observables for absolute viscosity, we seek to be able to put bounds on the relative and absolute viscosity values across the entire NA region, eastern upper mantle, and west upper mantle. The use of free-air gravity data instead of the corresponding geoid coefficients is well suited to constrain regional viscosity structure since free-air gravity data provide a more balanced representation of the different frequencies of the geopotential field (Mitrovica and Forte, 1997), especially from upper mantle source.

2.2 GIA models

Our GIA modeling approach follows the Maxwell viscoelastic realization of the mantle (Mitrovica and Peltier, 1991; Mitrovica et al., 1994). We calculate the pseudo-spectral Sea Level Equation (SLE) solved by the SELEN^4 (SealEveL EquatioN solver) code (Spada and Melini, 2019), originally based on the formulation of Farrell and Clark (1976), in a spherically symmetric gravitational and topographic self-consistent Earth model. The numerical implementation accounts for both rotational feedback and shoreline migration (Mitrovica and Peltier, 1991; Mitrovica and Milne, 2003). In our joint inversion analysis of mantle viscosity, we prescribe the viscoelastic love number with the TABOO model (Spada et al., 2011), which are used for the SLE

https://doi.org/10.5194/se-2021-151
Preprint. Discussion started: 4 January 2022

calculation with SELEN^4 via a probabilistic sampling.

We use the same a priori mantle layers for the GIA and mantle flow model (Fig. 2a). Using a nonlinear Bayesian inversion, we derive the absolute viscosity (η_a) structure by scaling the relative viscosity (η_r) profile of the regional mantle flow model by the Haskell (1935) value of 10^{21} Pa s at each Markov chain Monte Carlo (MCMC) iteration step. Each set of the joint inversion solutions runs on a single cluster node with 28 CPUs with a million iterations, consuming about 22,000 cpu hrs, while the relative viscosity-only inversions uses just about a fifth of the joint inversion cpu hrs. The rigidity and reference density values of the mantle layers in the postglacial modeling are based on PREM.
We employed two different ice thickness datasets for our study. Our first ice melting history is ICE-6G ice model (Peltier et al., 2015) concentrating on the North America Laurentide ice sheet components (herein referred to as ICE-6G-NA). We used the ice model of Tarasov et al. (2012) as a complementary second ice model which was derived with a statistical inversion for the North America region. At each step of the Marko Chain Monte Carlo simulation, we run the TABOO and SELEN^4 models with a proposed absolute viscosity (η_a), which is scaled from the regional mantle flow calculation or/and model uncertainty, and compare the resulting modeled relative sea level data to observations using a misfit function (see Sec. 2.3).

We use RSL data from Tushingham and Peltier (1991) global compilation database for the North America region (Fig. 2b). We based the regional continental inversions on RSL histories concentrated around Hudson Bay as shown in (Fig. 2d) to compare our results with previous GIA-only studies (Cianetti et al., 2002; Paulson et al., 2007). We restrict our ice melting history and RSL data to < 10 kyr BP. Here, the oldest RSL data point is used to normalize the younger data points in both the forward model predictions and observations to compute the misfit. Normalized RSL (NRSL) data was first introduced by (Mitrovica and Peltier, 1995) and also employed by Cianetti et al. (2002) in GIA studies for Hudson Bay. The main drawback for using NRSL is that any error in the oldest data point may translate into the remaining data points. However, this approach is best suited to isolate the effect of the regional viscosity from those related to the far field late Pleistocene surface ice load chronology (Cianetti et al., 2002; Mitrovica and Peltier, 1995).

2.3 Transdimentional Bayesian Inversion

Non-linear geophysical inversions based on Bayesian statistics have been used in a number of studies exploring Earth's physical properties to take advantage of the increasing availability and declining expense of computing resources (Tarantola and Valette, 1982; Green, 1995; Bodin et al., 2012). We employ a trans-dimensional hierarchical Bayesian inversion (Sambridge et al., 2013) for regional viscosity inversion by sampling the posterior probability density function $p(m|d_{obs})$ of a model (m) given observed data (d). Our modeled-observational data considered is either free-air gravity $(d[g])$ in the case of relative viscosity

https://doi.org/10.5194/se-2021-151
Preprint. Discussion started: 4 January 2022

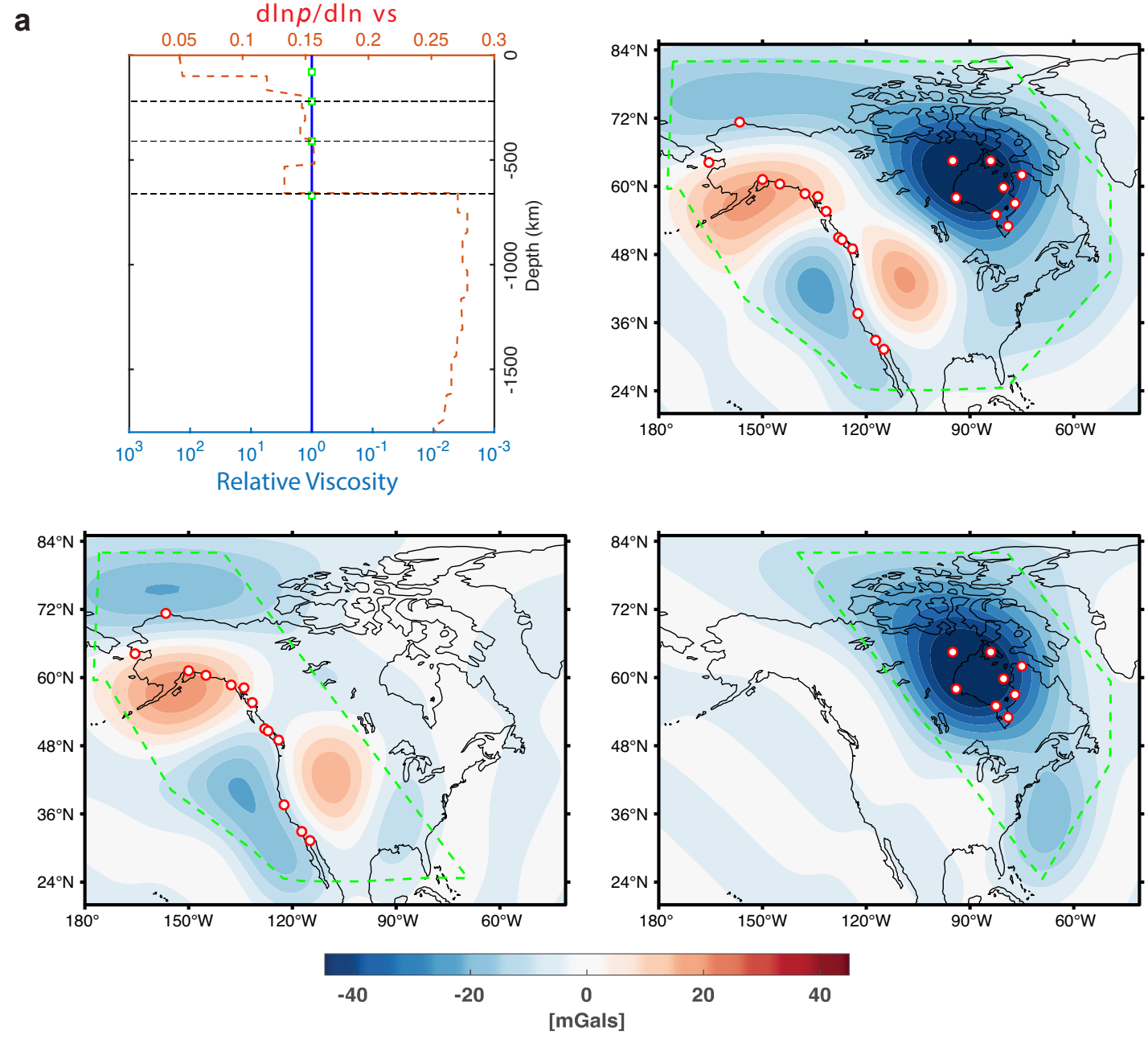

Figure 2. a) 1D isoviscous structure (blue line) with Voronoi nuclei (green squares) depicting our a prior mantle interfaces at 80, 220, 410 and 670 km. The red dash line shows seismic velocity to density conversion profile from Simmons et al. (2010). b–d) Localized free-air gravity observational data ($L = 2$ to 15) from the GRACE static field model Eigen-grace02s (Reigber et al., 2005) showing the b) entire North America region, c) Western Pacific region and d) Eastern cratonic region. The white dots with red outer rings are observed relative sea-level data sampled from Tushingham and Peltier (1991) for joint inversion analysis. Green dash lines showed the Slepian localization outlines R from Section 2.1.

https://doi.org/10.5194/se-2021-151
Preprint. Discussion started: 4 January 2022

constraints or a combination of free-air gravity and RSL data $(d[g, rsl])$ to constrain the absolute viscosity structure. We begin with Bayes' theorem for our model and data written as

$$p(m|d_{obs}) = \frac{p(d_{obs}|m) * p(m)}{p(d_{obs})} \tag{5}$$

The posterior distribution is proportional to the likelihood function $p(d_{obs}|m)$ and a prior probability density function $p(m)$. Since the data (i.e. evidence) given as $p(d_{obs})$ is independent of the model (m), we can rewrite the relation as:

$$p(m|d_{obs}) = p(d_{obs}|m) * p(m) \tag{6}$$

with the likelihood function given as

$$p(d_{obs}|m) = \frac{1}{\sqrt{(2\pi)^{n_{lm}}|M_d|}} \exp\left[-\frac{\Phi(m)}{2}\right] \tag{7}$$

We use the Mahalanobis distance misfit function $\Phi(m) = r^t M_d^{-1} r$ to measure the fitness of both the amplitudes and pattern between the observed data (i.e. free-air gravity field and relative sea level data) with the modeled residual data given as $r = d_{obs} - g(m)$. M_d is the covariance matrix and in our case we consider only a diagonal matrix to invert for the model uncertainties by employing distributions based on a Gaussian parametrization.

For each modeling setup, we start with a 1D isoviscous mantle with prescribed mantle layers/interfaces at 80, 220, 410 and 670 km (Fig. 2a) using Voronoi nuclei (Aurenhammer, 1991) and allow the viscosity values in the mantle layers to vary with respect to the prior information $p(m)$ expressed as a normal distribution. We use a reversible jump Markov chain Monte Carlo (MCMC) simulation where for each iteration step, our proposed relative viscosity structure η_r is obtained by varying an interface viscosity value at a random chosen depth/nodes. This is achieved by randomly picking any of the procedure Birth, Move, Value, and Noise change at equal probability to define the proposed candidate viscosity values at depth interfaces. Here, our 'Move' step is achieved by randomly picking and assigning viscosity value from one depth/node (e.g., η value below 670 km) to another depth (e.g., 410 km). The 'Birth' step predicts new viscosity values at a node chosen at randomly while 'Value' step alters viscosity value at a node, all based on the prior information.

The proposed viscosity structure is used to create our local geoid kernels which are convolved with the mantle's lateral density heterogeneities at each depth $\delta\rho_{lm}(r)$ in spherical harmonics, to synthesize the regional gravity signal in the spectral domain F_l^m. In the case of our joint inversion analysis, the proposed relative viscosity structure η_r used for predicting the local gravity field is then scaled to obtain our proposed absolute viscosity profile η_a for the GIA calculations component. The

https://doi.org/10.5194/se-2021-151
Preprint. Discussion started: 4 January 2022


Solid Earth Discussions

hierarchical step of the MCMC accounts for the data uncertainties. The solution at each iteration is accepted or rejected with a probability solution based on the Metropolis-Hasting algorithm with the proposed solution based on the minimization

$$min\left[1, \frac{p(m')}{p(m)}\frac{p(d|g')}{p(d|g)}\frac{n+1}{n'+1}\right]. \tag{8}$$

For each iteration step, a new local gravity response function is derived based on the perturbed viscosity and depth sampled from a prior distribution for the different MCMC procedure listed above, which can be accepted or rejected based on the previous solution. Compared to different inversion techniques, where a solution can converge in a local minima, our use of the Metropolis-Hasting algorithm helps to avoid such pitfalls, by searching the model and a priori information space.

2.4 Joint viscosity inversion from the local gravity and relative sea level data

We additionally combine our mantle flow calculations above with glacial isostatic adjustment modeling in a joint inversion calculation to infer local 1D absolute viscosity structure η_a. We base our analysis of the surface GIA effects on a multiple-1D basin specific rheological structure technique (e.g., Khan et al., 2016; Hartmann et al., 2020) and apply to the North America continental region as well as the east-west continental divide. Besides being less expensive computationally compared to global 3D finite element or finite volume GIA modeling, these authors' results suggest basin specific multiple 1D Earth models and ice loads could be more accurate than using single global 1D Earth structures to predict regional sea level rates and GIA fingerprints at different locations (Paulson et al., 2007).

We explore the lateral changes in viscosity between the eastern cratonic and western region upper mantle structures with our joint inversion. In the sub-regions we apply local ice melting histories for the GIA component similar to the Greenland analysis of Hartmann et al. (2020). In each case, the ice geometries are restricted to the region of interest by subgriding in space and time within the respective localization boundaries (see "R" in Eqn. 1) with the assumption that the respective local rheological structure is unique to the local GIA effect, the local ice sheet load and mantle structure below. We modify the Bayesian probability function to include the RSL data with the mantle convection data in our new residual matrix given as

$$r_{composite} = \begin{bmatrix} d_{gravity} - g_{gravity}[m]^i \\ \cdots \\ d_{gravity} - g_{gravity}[m]^n \\ : \\ \alpha * (d_{nrsl} - g_{nrsl}[m]^i) \\ \cdots \\ \alpha * (d_{nrsl} - g_{nrsl}[m]^n) \end{bmatrix} \tag{9}$$

https://doi.org/10.5194/se-2021-151
Preprint. Discussion started: 4 January 2022

where α represents a weighting of the RSL data. The error covariance matrix, assuming data uncertainties are given in the leading diagonal, has the form

$$M_d = \begin{bmatrix} \sigma_{gravity} & \cdots & 0 \\ \vdots & \ddots & \vdots \\ 0 & \cdots & \sigma_{nrsl} \end{bmatrix}. \tag{10}$$

We use a diagonal covariance matrix to reduce further complexity that may exist between the two data sets, in the case of a full covariance matrix. Our new likelihood misfit function for the joint inversion analysis therefore takes the form

$$p_{composite}(d_{obs}|m) = \frac{1}{\sqrt{(2\pi)^{n_{lm}}|M_d|}} \exp\left[-\frac{\Phi_{composite}(m)}{2}\right] \tag{11}$$

with the Mahalanobis distance misfit function given as

$$\Phi_{composite}(m) = r^t_{composite} M_d^{-1} r_{composite}. \tag{12}$$

We restrict the GIA calculations up to a maximum degree of $l_{max} = 36$, which is adequate for our regional statistical inversion (Cianetti et al., 2002) and also helps in speeding up our suite of calculations compared to the compute time using $l_{max} = 256$. As shown by Cianetti et al. (2002) the variation between GIA predictions (RSL) from including the additional degrees $l = 37$–256 are mostly within the bounds of data uncertainties. Paulson and Richards (2009) synthesis of the Hudson Bay postglacial data showed that the RSL data have most of their spectral content below spherical harmonic degree 30. For the mantle flow model component of the joint inversion, we focus on $l = 2$–15 in our discussion, and provide the results with $l =$ 2–10 in the appendix (Figure A6). The joint inversions follow the same procedure for determining total iterations and solution retention as our earlier calculations.

3 Results

3.1 Continent wide local relative viscosity solution

We apply our Slepian derived local geoid kernels for regional mantle flow calculations and Bayesian inversion simulation (MCMC) to infer a series viscosity profiles using the non-hydrostatic free-air gravity data as a constraint (Reigber et al., 2005). Our calculations are based in the spherical harmonics bandwidths from degree $l = 2$ to 10 and $l = 2$ to 15. We first examine the entire North America continental region to test the limits of the spectral localization technique before further localizing on the eastern and western regions to study more local viscosity structures. This allows us to evaluate the lateral changes in regional viscosity structure between the eastern cratonic region and the western shallow lithosphere structure as implied by the upper mantle thermal contrast (Yuan and Romanowicz, 2010). This also allows us to examine the ability of the local inversions to

https://doi.org/10.5194/se-2021-151
Preprint. Discussion started: 4 January 2022

Solid Earth
Discussions
Open Access
EGU

detect and identify viscosity values and/or upper mantle interfaces that are robust with regards to the localized seismic-derived density model.

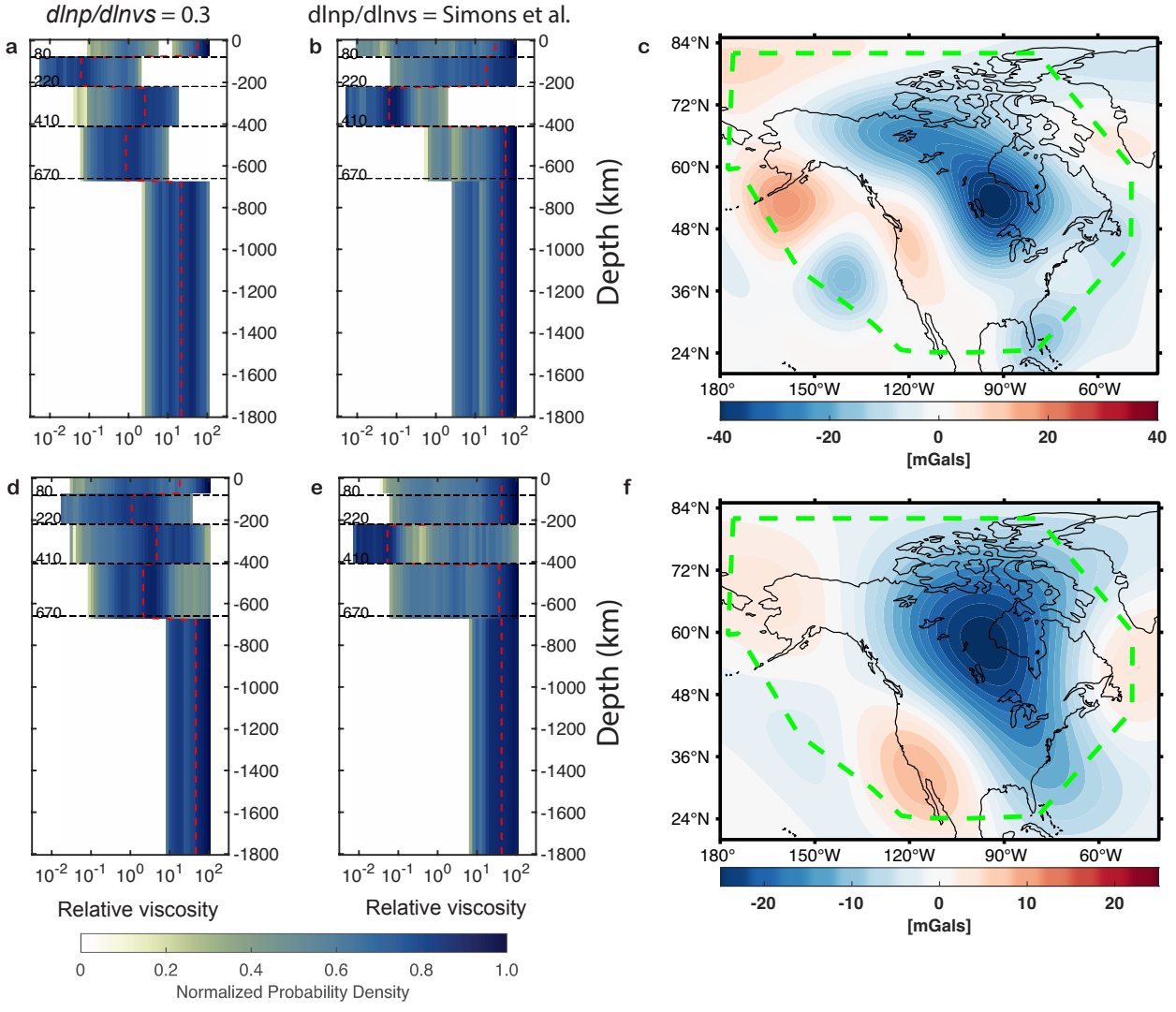

Figure 3. Ensemble of regional relative viscosity solutions of North America continental region for spherical harmonic degree (a-b) L =2 to 15 and (d-e) L =2 to 10. The left column is based on seismically-derived mantle model from (French and Romanowicz, 2015) using constant seismic velocities to density scaling of 0.3 and the right column with depth-dependent scaling parameters from (Simmons et al., 2010) (Fig. 2a, dashed red line). The dash red lines in each panel shows the average viscosity from each solution. Horizontal dash black lines are our a prior mantle interfaces used in our MCMC inversions. The averages of the resulting modeled free-air gravity field, which are ensemble from the MCMC calculation are shown in **c** for L =2 to 15 and **e** for L =2 to 10.

https://doi.org/10.5194/se-2021-151
Preprint. Discussion started: 4 January 2022

In Fig. 3, we show 2D histograms of our viscosity solutions for $l = 2$ to 15 (panels a, b) and $l = 2$ to 10 (panels d, e), sampled from MCMC simulations using constant (left column) and depth-dependent (right column) seismic velocity-to-density scalings (Fig. 2a, dashed red line) in the regional forward mantle flow calculations. We obtain a low viscosity channel below the lithosphere for constant scaling ($\delta ln\rho/\delta lnv_S = 0.3$) (Fig. 3 a & d) while a strong yet somewhat deeper asthenospheric interface is inferred with the depth-dependent scaling profile (Fig. 3 b & e) (Simmons et al., 2010). Using a smaller constant velocity-density conversion parameter of $\delta ln\rho/\delta lnv_S = 0.15$ resulted in similar viscosity values to the depth-dependent profile of Simmons et al. (2010) (see Appendix Figure A2).

We obtain a relatively a weaker viscosity interface above the 410 km mantle layer with seemingly no clear viscosity change at the 670 km with the Simmons et al. (2010) depth-dependent seismic-to-density parameter scaling profile (also with $\delta ln\rho/\delta lnv_S$ =0.15). In contrast, the high velocity-density scaling parameter of $\delta ln\rho/\delta lnv_S = 0.3$ gives a small viscosity change at the 410 km and a large viscosity jump at the 670 km seismic interface, that in total result in about one order of magnitude viscosity increase between the upper (i.e. above 670km) and lower mantle. All of our local mantle viscosity solutions resulting from the different seismic scalings or spherical harmonic spectrums considered here show strong mid-to-lower mantle viscosity values. Differences in our inferred 1D regional viscosity are more dependent on the seismic-to-density scaling used than the spectral bandwidths considered.

We show the corresponding final averages of the modeled free-air gravity field obtained from the MCMC simulations for $l =$ 2 to 15 (Fig. 3 c) and $l = 2$ to 10 (Fig. 3 f). These show low amplitudes compared to the corresponding observed data (Fig. 2b), with the Hudson Bay negative gravity anomaly showing minimum values of roughly -30 to - 20 mGals for $l = 2$ to 15 and $l =$ 2 to 10, respectively. These averaged free-air gravity fields are not true gravity solutions and may also not be reproducible from the respective resulting average 1D viscosity (Fig. 3a & Fig. 3d, red dashed lines) (e.g., Rudolph et al., 2021). The $l = 2$ to 15 free-air gravity field (Fig. 3 c) gives a variance reduction of 40.35% and a correlation coefficient of 0.59 with the observed gravity field (Fig. 2b) while the corresponding $l = 2$ to 10 gravity field average (Fig. 3 f) gave a variance reduction of 50.22% and a correlation coefficient of 0.69.

3.1.1 Western NA+Pacific and Eastern cratonic relative viscosity structures

We further localize the North America continental region into east and west regions to examine the respective local viscosity characteristics of the eastern cratonic and western cordilleran regions (Fig. 4). We test the same seismic velocity-to-density scalings parameters used in the above calculations. Each local viscosity solution shows the influence of the respective upper mantle structure, with the western shallow hot mantle heterogeneities (Fig. 4 a,b) and the corresponding eastern cold continental root (Fig. 7 c,d) resulting in distinct upper mantle viscosity characteristics compared to the continent-wide viscosity solution. Regardless of the seismic velocity-to-density scaling used, the dominate thermal/density heterogeneities of each region dictate the rheological behavior seen in the upper mantle. Using the spectral localization techniques we are able to examine each region's local viscosity profiles and minimize the lateral effects between the eastern and western upper mantle structures.

https://doi.org/10.5194/se-2021-151
Preprint. Discussion started: 4 January 2022

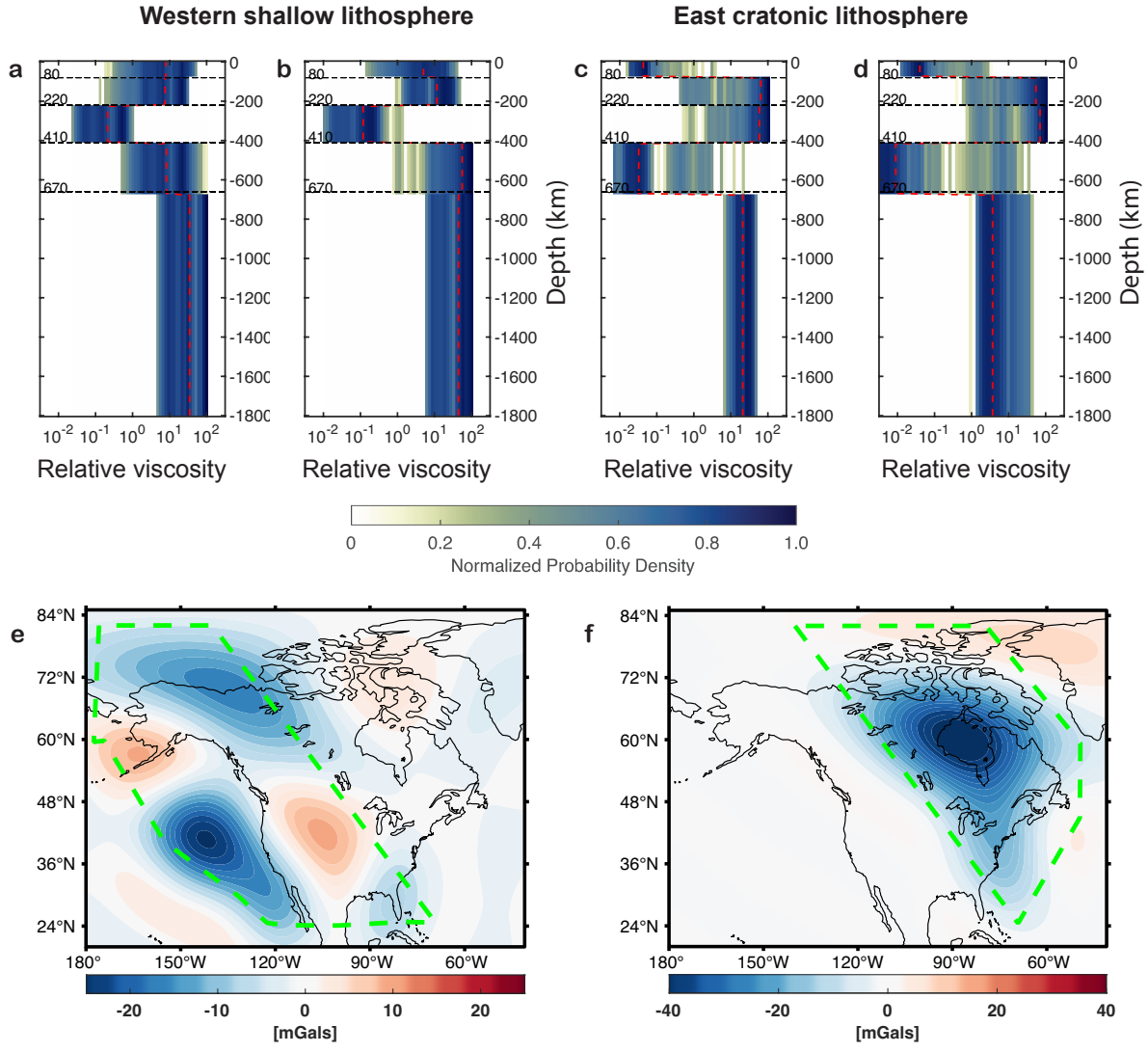

Figure 4. Ensemble local relative viscosity solutions showing the (a-b) Western Pacific and (c-d) Eastern cratonic regions of North America for spherical harmonic degree L =2 to 15. The panels **a** and **c** are based on seismically-derived mantle model from French and Romanowicz (2015) using constant scaling of 0.3 while panels **b** and **d** are based on depth-dependent scaling from Simmons et al. (2010). In each plot the dashed red line shows the average resulting viscosity for the region. Horizontal dash black lines are our a priori mantle interfaces used in our MCMC inversions. **e** and **f** show the free-air gravity averages for the Western NA+Pacific and Eastern cratonic regions respectively, ensemble from the MCMC solutions for **c** for L =2 to 15 and $\delta ln\rho/\delta lnv_S = 0.3$.

https://doi.org/10.5194/se-2021-151
Preprint. Discussion started: 4 January 2022

In the eastern cratonic region, we infer a strong viscosity interface at 410 km depth, moving from a strong upper mantle to a very weak transition zone as depth increases. This aligns with the approximate depth range of the region's proposed continental root extending to about 250–350 km depth (Aktas and Eaton, 2006; Yuan and Romanowicz, 2010). The resulting mean eastern gravity field gave a variance reduction of 80.20%. We examine this in more detail in our joint inversion solution including RSL data in the Hudson Bay region.

In contrast, the western part of the NA mantle gives relatively low viscosity below the lithosphere extending down to 410 km depth. Both seismic scalings gave roughly a factor of 100 viscosity jump across the transition zone (from above 410 to below 670 km) with the main difference being wether it all occurs at 410 km depth (Fig. 4 b) or if it is evenly spread between similar jumps at 410 and 670 km depth (Fig. 4 a). The depth-dependent scaling resulted in similar viscosity interfaces at the 670 km (or lack thereof) for both spectral bandwidths considered with $L = 2 - 15$ shown in Fig. 4 b ($L =$ 2-10 solutions not shown).

3.2 Joint viscosity inversions from local dynamic and postglacial modeling

3.2.1 Continent wide viscosity solution

We combine the above local mantle flow calculations and the postglacial modeling code SELEN^4 (Spada and Melini, 2019) in a joint inversion analysis (Eqn. 11) to infer absolute viscosity structure (η_a). We consider two regionally synthesized spatio-temporal surface ice loads including ICE-6G (Peltier et al., 2015) and GLAC1D-NA Tarasov et al. (2012) for the North America region. We first apply our joint inversion analysis to infer viscosity (ηa) for the entire NA continental area (Fig. 5) similar to our relative viscosity (η_r) solution from gravity alone (Fig. 3), before moving on to eastern and western NA solutions.

In Fig. 5a, we show a 2D histogram of the regional viscosity structure inferences for spherical harmonic degrees $l = 2$ to 15 based on the depth-dependent velocity-density conversion profile from Simmons et al. (2010) (Fig. 2a, dashed red line) in the mantle flow model and with ICE-6G-NA ice histories for the GIA modeling. Panels Fig. 5**b** and **c**, show solution averages for different seismic-density scalings and different weightings of GIA data in the inversions (Eqn. 9).

We inferred an average viscosity of 10^{21} Pa s in the entire upper mantle above the 670 km seismic discontinuity with a low viscosity channel of about 0.75 - 1 x 10^{20} Pa s between the depth range of 220 km and 410 km (Fig. 5a, b – solid lines). In these calculations the transition zone viscosity is similar to the lower mantle viscosity below 670 km. With the constant velocity-density conversion of $dln\rho/dlnvs = 0.3$, we obtained a monotonic viscosity increase with depths below the lithosphere, generating about one order of magnitude viscosity jump at the 670 km (Fig. 5 b & c dashed lines). Both scenarios gave similar lower mantle viscosity, ranging between 1 - 2 x 10 ^{22} Pa s.

Our regional mantle viscosity results based on the depth-dependent velocity-density scaling profile (Simmons et al., 2010) favors a strong mantle interface at the top of the mantle transition zone (Fig. 5a, 5 b solid lines) with seemingly a lack of viscosity jump at the 670 km. Recently, Mitrovica et al. (2015) and Lau et al. (2016) used various GIA data in viscosity inversions and showed that a GIA derived viscosity structure doesn't necessary require the 670 km viscosity jump to fit observational

https://doi.org/10.5194/se-2021-151
Preprint. Discussion started: 4 January 2022

Solid Earth
Discussions
Open Access
EGU

data. On the other hand, inversion results based the constant scaling of $dln\rho/dlnvs = 0.3$ give a clear viscosity contrast between the mantle transition zone and the lower mantle as seen in other work (e.g. King, 2016; Davies, 1995). Our two sets of joint inversion solutions do reasonably good job matching model and observational RSL data (Fig. 7 and Figure A3), even
300 though they distinctively predict different 670 km mantle viscosity interfaces (Fig. 5 b, solid and dashed lines), as well as depth differences of the low viscosity zone below our 80 km imposed elastic lithosphere.

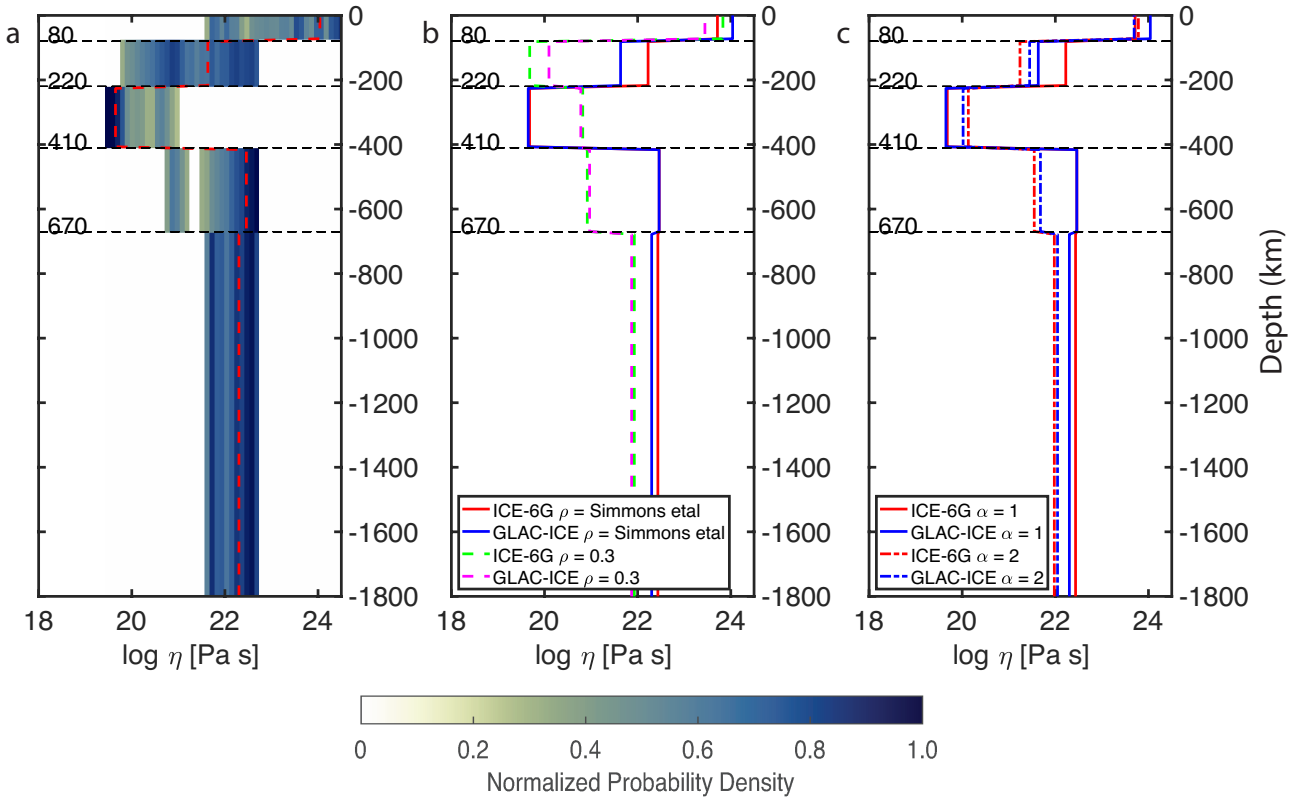

Figure 5. Continent wide local joint inversion of mantle viscosity showing (**a**) Ensemble 2D histogram of viscosity solution of North America based on seismically-derived local mantle density (i.e. SEMUCB-WM1 seismic model from French and Romanowicz (2015)) with depth-dependent scaling profile from Simmons et al. (2010). (**b**) Mean regional viscosity profiles using constant velocity-density conversion parameter (dash lines) and depth-dependent Simmons et al. (2010) (solid lines). (**c**) Similar to Figure 5b depth-dependent seismic scaling with a weighting parameterization of α = 2 applied to the postglacial component of the joint inversion. The horizontal dash black lines are our imposed a priori mantle interfaces for the MCMC inversions with constant elastic lithosphere of 80 km and an asthenospheric depth at 220 km, followed by the 410 and 670 km seismic mantle interfaces.

The two different regional deglaciation models (ICE-6G-NA and GLAC1D-NA) employed for the joint inversions show little influence on viscosity values obtained among the series of solutions (Fig. 5b & c). Rather, the choice of the mantle seismic velocity-density scaling parameterization shows a stronger degree of influence on the upper mantle viscosity structure. To

https://doi.org/10.5194/se-2021-151
Preprint. Discussion started: 4 January 2022

better understand the significance of our findings in line with our joint inversion formulation and our initial model parameterization, we explore a different weighting (Eqn. 9) to the GIA data to evaluate a new set likelihood function and viscosities. By doing this we seek to evaluate any bias that may stems from either our mantle flow and/or postglacial RSL data in our misfits estimations and the corresponding viscosity values.

We apply a weighting the $\alpha = 2$ in Eqn. 9 to the GIA data considering our two ice melting histories and compare the resulting upper mantle viscosity values with those that have no weighting applied. For comparison, we show in Fig. 5c (solid lines) the results from applying a weighting of $\alpha = 2$ combined with the Simmons et al. (2010) velocity-density scaling for the mantle flow. The most obvious impact is a small viscosity jump at the 670 km and a reduction of the low viscosity channel at the 410 km, giving an uplift of 8-10 mm/yr (see Figure A3) compare to the results without a weighting (i.e., $\alpha = 1$) shown in Fig. 5b (solid lines), predicting uplifts in excess of 2-3 mm/yr (see Fig. 7).

3.2.2 East and West local joint viscosity inversion

Similar to our flow-only inversions, we perform additional joint inversions for the eastern and western sub-regions of North America. The sub-regional joint inversion for the western part of NA, with (Simmons et al., 2010) seismic-density scaling, shows a gradual viscosity increase with depth (Fig. 6a) below 220 km depth. We obtain a weak upper mantle layer with viscosity at the 410 km averaging at 0.8 x 10^{21} Pa s and a slight increase in the mantle transition zone showing 1-3 x 10^{21} Pa s (Fig. 6a). Compared to previous postglacial and mantle viscosity studies of the western Pacific coast (e.g., James et al., 2000, 2009b, a), we inferred a relatively high asthenospheric viscosity with our joint inversion resulting in a much higher uplift of approx. 5-7 mm/yr (Fig. 6d), about 10 times higher than observed values. Here, we did not take into account tectonic effects due to seismic activities, which was shown to be a larger component (James et al., 2009b; Yousefi et al., 2018, 2021) of the regions RSL data, showing our poorly fit model predictions. We discuss the set of resulting RSL predictions for our model parameterization and assumptions with limitation and future directions in the discussion (Sec. 4).

Eastward, our joint inversion for the cratonic NA sub-region shows strong viscosity above the 410 km mantle layer, averaging at about 10^{22} Pa s (Fig. 6b) based on Simmons et al. (2010) profile. The inferred high asthenosphere viscosity values is similar to lower mantle viscosity 10^{22} Pa s. We also tested seismic-density scaling of $\delta ln\rho/\delta lnv_S = 0.3$ for both the eastern regional joint inversions, but the impact of the eastern cratonic structure still shows a large influence on the resulting mantle viscosity above 410 km, giving a strong contrast in viscosity values between the east and west of about 2 orders of magnitudes within the same mantle layers. The continent-wide viscosity solution (Fig. 5), seemingly the average of the east-west local inversions is more closer to the west local 1D profile within the depth range of the continent keel.

https://doi.org/10.5194/se-2021-151
Preprint. Discussion started: 4 January 2022

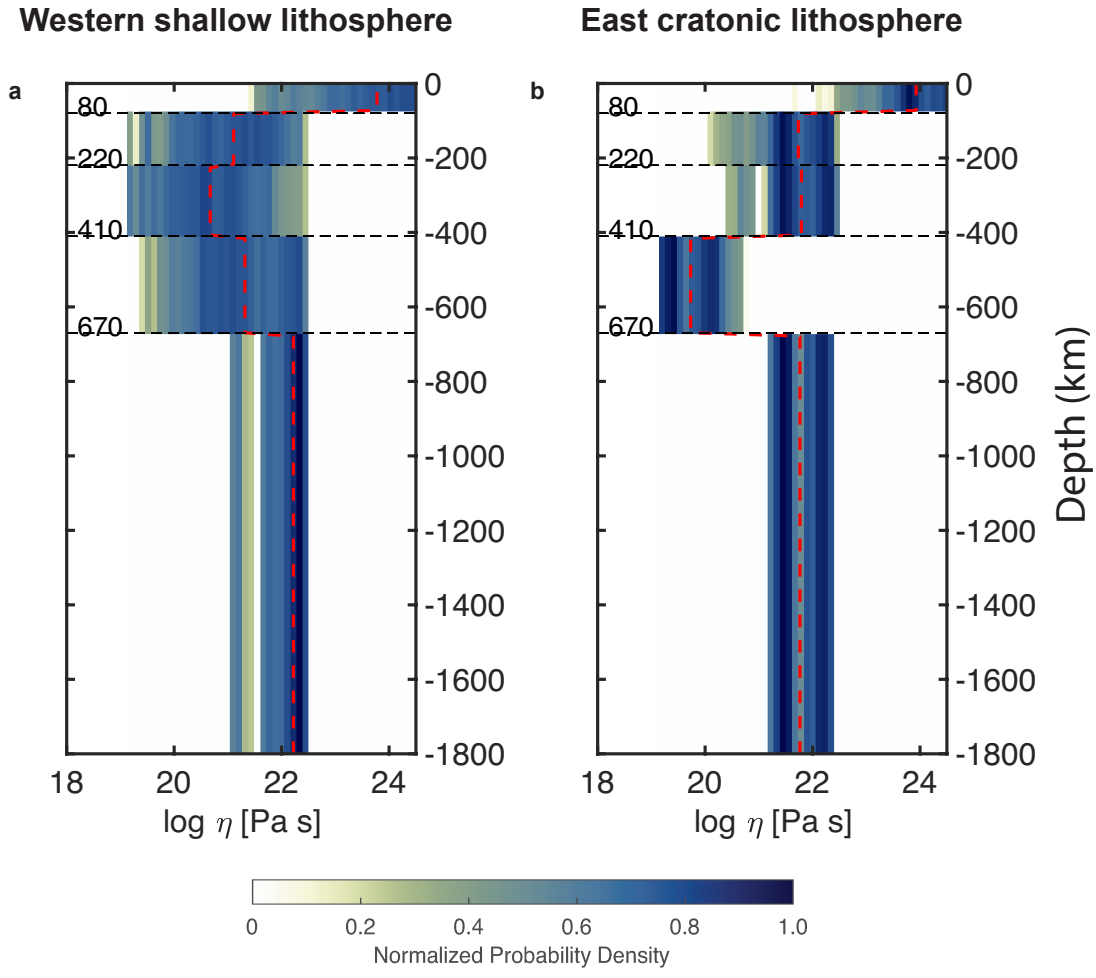

Figure 6. Ensemble of western shallow lithosphere (**a**) and eastern cratonic (**b**) local mantle viscosity solutions of North America for spherical harmonic degree L =2 to 15 using seismically-derived mantle model from French and Romanowicz (2015) with constant scaling of 0.3. The dash red lines in each panel shows the average viscosity for the region. Horizontal black lines are the imposed mantle interface in our MCMC inversions to distinguish our constant lithosphere of 80 km and Asthenospheric channel, followed by the 410 and 670 km seismic mantle interfaces.

https://doi.org/10.5194/se-2021-151
Preprint. Discussion started: 4 January 2022

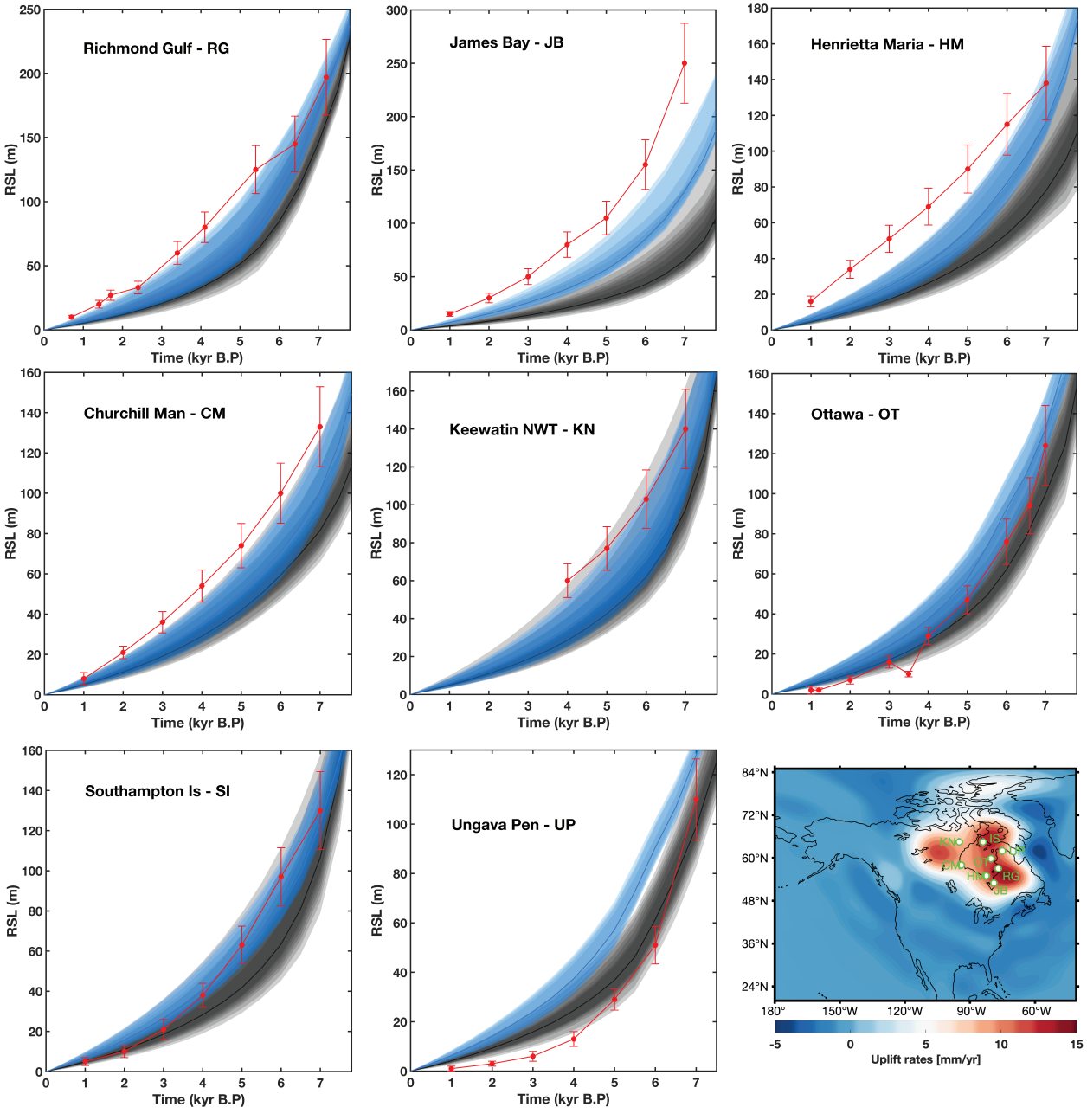

Figure 7. Ensemble RSL predictions from our joint inversion considering the entire NA continental area. The blue shades correspond to our viscosity inference with the locally synthesized deglaciation model ICE-6G (Peltier et al., 2015) which the dark shades are based on GLAC1D-NA ice sheet model Tarasov et al. (2012) for the North America region. The respective red lines with σ error bars are the observed relative sea level for the Hudson Bay. Each panel shows a plot of RSL heights in meters against time in 1000 years. The lower right conner map shows the resulting postglacial average uplift sampled from a few 1000s iterations at the end of the joint inversion with RSL sites name ID in green. The mantle flow component of the joint inversion used the Simmons et al. (2010) seismic conversion profile in both calculations.

https://doi.org/10.5194/se-2021-151
Preprint. Discussion started: 4 January 2022

335 ## 4 Discussion

4.1 Continent-wide and east-west local 1D viscosity (η_r and η_a).

The North America continental area is influenced by ongoing dynamic adjustment to the effects of the now disappeared Laurentide ice sheet (e.g., Mitrovica and Peltier, 1995), mantle convection (Simons and Hager, 1997, .e.g,) as well as prior subduction history. These geodynamics processes are largely controlled by the viscosity of the mantle. Our regional relative viscosity (η_r)
340 inversion results based on free-air gravity data for the North America continental area (NA) show either a weak or strong channel below the lithosphere and a similar behavior at the transition zone, due to the modeling parameterization considered.

Particularly, our choice of velocity-density scaling parameter for the local seismic model in the forward model calculations primarily dictate the characteristics of the viscosity solution compared to the different spectral bandwidths considered, espe-
345 cially within the upper mantle (Fig. 3). Regional seismic studies of the NA continental area (Yuan and Romanowicz, 2010) show the upper mantle structure is characterized by shallow slow seismic anomalies in western NA, contrasted by fast anomalies in the shallowest 200 – 300 km of the eastern cratonic region. The inference of the continent-wide weak asthenospheric viscosity with $\delta ln\rho/\delta lnv_S = 0.3$ (Fig. 3 a, d) seismic scaling suggest large velocity-density conversion parameters favor dominance by hot mantle material. This is evident as the western shallow hot mantle material largely dictates the resulting asthenosphere av-
350 erage viscosity as opposed to the corresponding the cold eastern cratonic region. The non-linear petrological relation between mantle densities and seismic velocities (Forte and Peltier, 1991; Simmons et al., 2010) affect thermal and non-thermal mantle materials at depths and lateral extent differently, making our choice of either single value or depth-dependent scaling parameter less effective in resolving the mantle's lateral thermal/compositional variations to constrain viscosity for the entire continent.

355 In our continent-wide viscosity analysis for both η_r and η_a, there is more than one order of magnitude inferred viscosity difference within the transition zone between considering either $\delta ln\rho/\delta lnv_S = 0.3$ (e.g., Fig. 5 dashed lines) or the Simmons et al. (2010) depth-dependent seismic density scaling profile (e.g., Fig. 5 solid lines). Our results fall into the two groups of hard and weak transition zone viscosity profiles proposed by King [1995] that can reproduce the observed geoid/gravity. Though none of the continent-wide viscosity solutions give a weaker transition zone (e.g., Mitrovica and Forte, 2004) with respect to
360 the upper mantle (above 410 km) but are more in line with the findings of Hager and Richards (1989) global mantle flow studies.

In the case of our sub-regional eastern 1D viscosity structure (Fig. 4c, d and Fig. 6b) we inferred an ultra low viscosity channel in the transition zone is similar to Liu and Zhong (2016) thermochemical mantle model with no restriction on their upper mantle and transition zone viscosity parameterization. Mantle viscosity inversion by King and Masters (1992) showed very low
365 transition mantle viscosity. Compared to previous global mantle flow studies (King and Masters, 1992; Liu and Zhong, 2016) and joint inversions (Mitrovica and Forte, 2004) giving low transition zone viscosity, only our eastern NA local inversions show such a weaker layer, while the western NA or continent-wide inversion resulted in a moderately weak channel with about an order of magnitude jump between transition zone and the lower mantle. This depth is sandwiched between the tail end of the

https://doi.org/10.5194/se-2021-151
Preprint. Discussion started: 4 January 2022

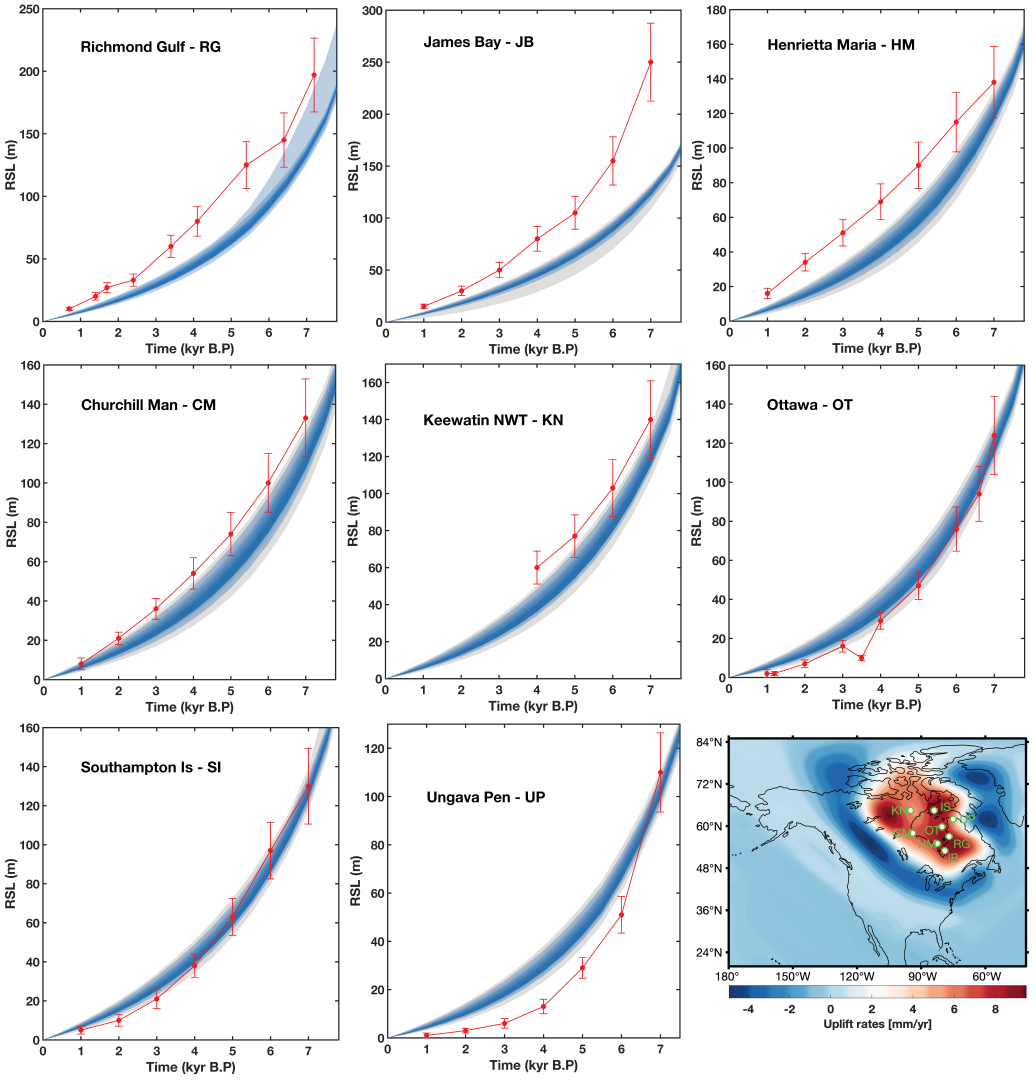

Figure 8. Ensemble RSL predictions from our joint inversion for the NA cratonic region. The shaded profiles correspond to our viscosity inference with the locally synthesized deglaciation model GLAC1D-NA Tarasov et al. (2012) . The respective red lines with σ error bars are the observed relative sea level for the Hudson Bay. Each panel shows a plot of RSL heights in meters against time in 1000 years. The lower right conner map shows the resulting postglacial average uplift sampled from a few 1000s iterations at the end of the joint inversion with RSL sites name ID in green. The mantle flow component of the joint inversion is based on $dln\rho/dlnvs = 0.3$ as a seismic conversion factor.

https://doi.org/10.5194/se-2021-151
Preprint. Discussion started: 4 January 2022

Farallon slab and the cratonic root. We think such a localized ultra low viscosity channel could be a combination of hot mantle materials displaced/pushed and assembled above the descending Farallon slab (Camp et al., 2017) and fluids/volatiles as the Farallon slab dehydrate due high mantle temperatures and pressure that found their way into the mantle transition zone (Ohtani et al., 2018). Such ultra low viscosity within the transition zone may contribute to the short relaxation time for the Husdon Bay region compared to the longer Fennoscandian relaxation time (Wieczerkowski et al., 1999), even though both postglacial rebounds are occurring on an Archean continental region.

Large-scale mantle convection studies based on seismic tomography models with different velocity-density scaling parametrization, petrochemical, and thermal assumptions (Steinberger and Calderwood, 2006; Liu and Zhong, 2016; Simmons et al., 2010) have shown a variety of viscosity values across depths and varied conclusions on viscosity magnitudes. Using the spectral localization inversion, we are able to show how regional slow and fast seismic anomalies, translating into mantle density heterogeneities influences the resulting viscosity profiles (Fig. 4) at continent-wide (Fig. 3) or sub-continental (Fig. 4) scale compared to global mantle flow 1D viscosity inversions (Rudolph et al., 2015; Liu and Zhong, 2016; Steinberger and Calderwood, 2006). The conventional scaling of seismic velocity to densities for mantle flow calculations leads to different results when fast and slow mantle materials are scaled independently, resulting in different rheological values. This should inform the importance of devising a new way of lateral seismic velocity to density scalings in mantle flow studies.

Other factors such as data resolution and local spectral analysis may influence our local results compared to global studies. Here, our regional viscosity inferences for the eastern and western mantles provides insight into the viscosity contrast between the cratonic east and western NA+Pacific shallow mantles, serving a a first order constraint on the NA continental region's lateral viscosity variations (Ghosh et al., 2010). The different values of seismic velocity-to-density scaling parameterization of the hot and cold anomalies of the mantle dominate our mantle viscosity results in the continent wide inversion compared to less influence in the east-west respective inversions. Other factors such as asthenospheric partial melting (Karato and Wu, 1993) or chemical depletion within the continental keel (Jordan, 1988; Pari and Peltier, 1996) will further influence the upper mantle viscosity. Overall, the NA regional upper mantle is complex as the region accommodates strong continental root (Jordan, 1988; Yuan and Romanowicz, 2010), dynamics of the Farallon slab (Forte et al., 2010), and some degree of asthenospheric melting from the thermally buoyant Yellowstone plume ascension about 16 Ma ago through a fractured region of the Farallon plate (Camp et al., 2017). With the caveat that viscosity inversion is a non-unique problem and there are often tradeoffs between viscosity and depth, it is worth noting that in many cases our inversion probability density distributions between the east and west regions do not overlap, and there are clear geophysical arguments that justify deeper low viscosity channels under cratonic roots.

4.1.1 RSL model predictions

The set of RSL predictions resulting from our continent wide viscosity joint inversion (Fig. 7) show varying degrees of misfits between model results and observations due to the preferred regional viscosity values, the ice sheet models, and the site spe-

https://doi.org/10.5194/se-2021-151
Preprint. Discussion started: 4 January 2022

cific relative sea-level data. The average RSL estimates from the ensemble are depicted as deep blue/dark lines with a shaded region around and the respective observed RSL data used to constrain our viscosity inversion are the red lines for each site sampled in the Hudson Bay. While the fit between observed and the predicted means at sites north of the Hudson Bay such as Ottawa, Southampton, and Keewatin (Fig. 7), are within the data error bounds with both deglaciation models GLAC1D-NA and ICE-6G-NA, sites like the James Bay and Henrietta Maria show large misfits between the modeled and observed RSL data.

None of the continent wide joint inversion viscosity solutions with averages 10^{21} Pa s and 10^{22} Pa s in the upper and lower mantles respectively (Fig. 5b) were able to fit all the RSL data well simultaneously, regardless of the seismic density scaling or the ice model used. This also applies to the inversion scenario where we increased weighting (Fig. 5c, solid lines and see Appendix Figure A3 for RSL) of the GIA component of the joint inversion. Comparing both ice sheets models used, RSL predictions using the GLAC1D-NA ice model (Fig. 7) dark shades fit more poorly than those using the ICE-6G-NA model, with the exception of the Ungava Peninsula RSL site.

Glacial isostatic adjustment studies by Nakada and Lambeck (1989) and Mitrovica and Peltier (1995) in the Hudson Bay region show that a subset of the region's relative sea-level data imply lower viscosity values than the remaining sites. Particularly, their results showed that the Henrietta Maria RSL site favors models with a lower mantle viscosity of 3 x 10 ^{22} Pa s, which is about an order of magnitude higher than our inversion results. A weaker viscosity channel below the lithosphere (80 km) obtained with using $dln\rho/dlnvs = 0.3$ as seismic conversion factor does a better job with James Bay and Henrietta Maria RSL sites but deteriorate the fits in Ottawa and Ungava Peninsula (see Appendix Figure A4). Our lower mantle viscosity average of 10^{22} Pa s is about an order of magnitude more than the findings of Cianetti et al. (2002) based on GIA inversion alone. Though we obtain similar hard and soft transition zones based on our seismic scalings, none of our transition zone showed high viscosity with respect to the lower mantle Cianetti et al. (2002). Note that our spectral localization technique combined with the basin specific regional GIA modeling approach is likely less effective at constraining deep/lower mantle viscosity values, due to a decrease in sensitivity of our localization technique with depth for small regions. Compared to the findings of (Forte and Mitrovica, 1996) our choice of the regional seismic density scaling shows large influence on the resulting local 1D viscosity especially in the continent wide upper mantle, though there seems to be little to no effect on the corresponding RSL predictions.

Our eastern joint inversion in the Hudson Bay area fits of the observed RSL data, with the exception of James Bay and Henrietta Maria sites (Fig. 9). The ensemble RSL show more narrow bands suggesting tight sampling of the parameter space for the RSL predictions. The resulting upper mantle viscosity above 410 km is exceptionally high 10^{22}Pa s (Fig. 6b), comparable to the lower mantle viscosity as also found by Kaufmann and Lambeck (2002) in the joint inversion study. However, the ensemble RSL data predictions of the western local joint inversion do a poor job fitting the observed data with upper mantle average viscosity of 0.8 to 1.0 x 10^{21} Pa s. Compared to previous GIA only studies of the region (Yousefi et al., 2018, 2021), which accounted for slab morphology and tectonic effects, our mantle flow component of the joint inversion can not decipher the regional tectonic influence on the RSL. The use of a global seismic tomography model (French and Romanowicz, 2015)

https://doi.org/10.5194/se-2021-151
Preprint. Discussion started: 4 January 2022

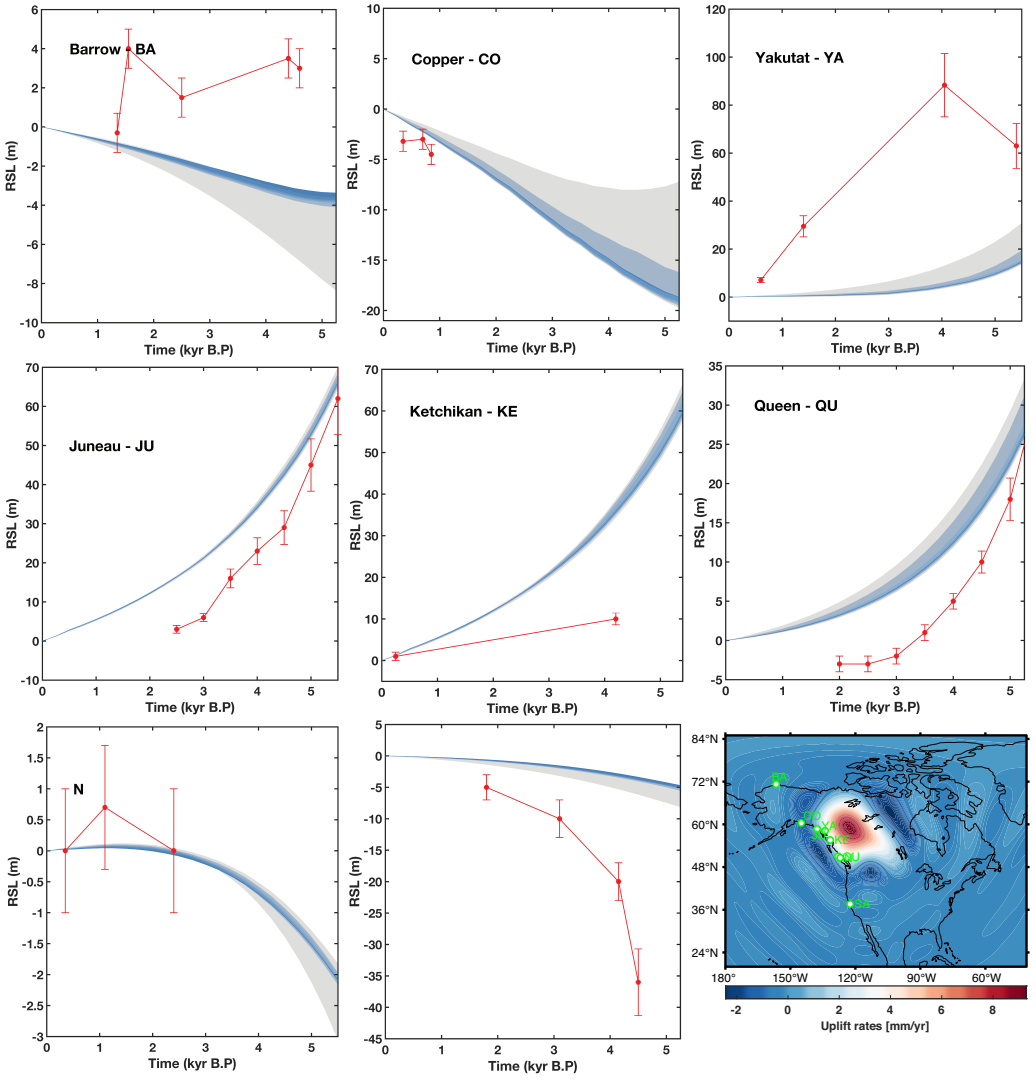

Figure 9. Ensemble RSL predictions from our joint inversion for the West region of NA. The shaded profiles correspond to our viscosity inference with the locally synthesized deglaciation model GLAC1D-NA ice sheet model Tarasov et al. (2012). The respective red lines with σ error bars are the observed relative sea level. Each panel shows a plot of RSL heights in meters against time in 1000 years. The lower right conner map shows the resulting postglacial average uplift sampled from a few 1000s iterations at the end of the joint inversion with RSL sites name ID in green. The mantle flow component of the joint inversion is based on $dln\rho/dlnvs = 0.3$ as the seismic conversion factor.

https://doi.org/10.5194/se-2021-151
Preprint. Discussion started: 4 January 2022

with local resolution deficiencies could be a major factor, as well as our use of uniform lithosphere without a crustal structure. Future studies will test regional tomography models based on the US array. The different seismic density scalings showing different realizations of the regional viscosity did not improve the RSL model fit.

5 conclusion

We use local geoid kernels based, created with Slepain localization basis functions, to infer regional mantle viscosity using either free-air gravity or/and relative sea level data via a Bayesian inversion for the North America continental region. We explored a series of relative and absolute viscosity inversions by testing different seismic velocity to density scaling parameters and ice melting histories.

The most important parameter on the resulting local viscosity is the value of velocity-density conversion factor, irrespective of the spectral bandwidth considered or the glacier ice model used. We obtain an order of magnitude relative viscosity increase between the upper mantle (i.e. above 670 km) and the lower mantle when we used $dln\rho/dlnvs = 0.3$ conversion factor. These translated into a corresponding upper mantle and lower mantle viscosities of 10^{21} and 1-2 x 10^{22}Pa s, respectively in our joint inversion the entire NA continental region. In the case of depth-dependent seismic scaling from Simmons et al. (2010), the mantle transition zone show a stiff interface and in most cases shows viscosity values similar to those the lower mantle.

Testing our spectral localization technique on eastern cratonic and Pacific west regions revealed a contrary conclusion to our continent-wide inversions. Our new sets of east-west local inversions showed that the respective mantle heterogeneities control the resulting viscosity characteristics, with less influence of the choice of mantle density conversion factor. The 1D local viscosity from the eastern region viscosity analysis show a strong upper mantle correlating with the craton depth range (between 200 to 300 km), while the Pacific west 1D viscosity structure show a gradual increase with depth below the 220 km depths. The relative sea level predictions do not fit the corresponding observations well especially in the case of the western local inversion. Including other GIA data sources in the inversion or for validation may improve the current study or a consideration of lateral viscosity variations.

By focusing on a single seismic model (French and Romanowicz, 2015) for the NA continental area with the sub-regions for our viscosity inversion, we are able to explore/isolate heterogeneous and/or homogeneous mantle material through seismic-velocity scalings and interpret the intrinsic behavior/characteristics on inferred viscosity values which will be very difficult in global flow models. Our results also show the need consider lateral mantle seismic-velocity scalings in global flow models especially in the upper mantle below continents.

Code and data availability. We make our code and data available on the following Github pages (https://github.com/oseitutu) and (https://github.com/harig00)

https://doi.org/10.5194/se-2021-151
Preprint. Discussion started: 4 January 2022

Solid Earth
Discussions
Open Access
EGU

Appendix A

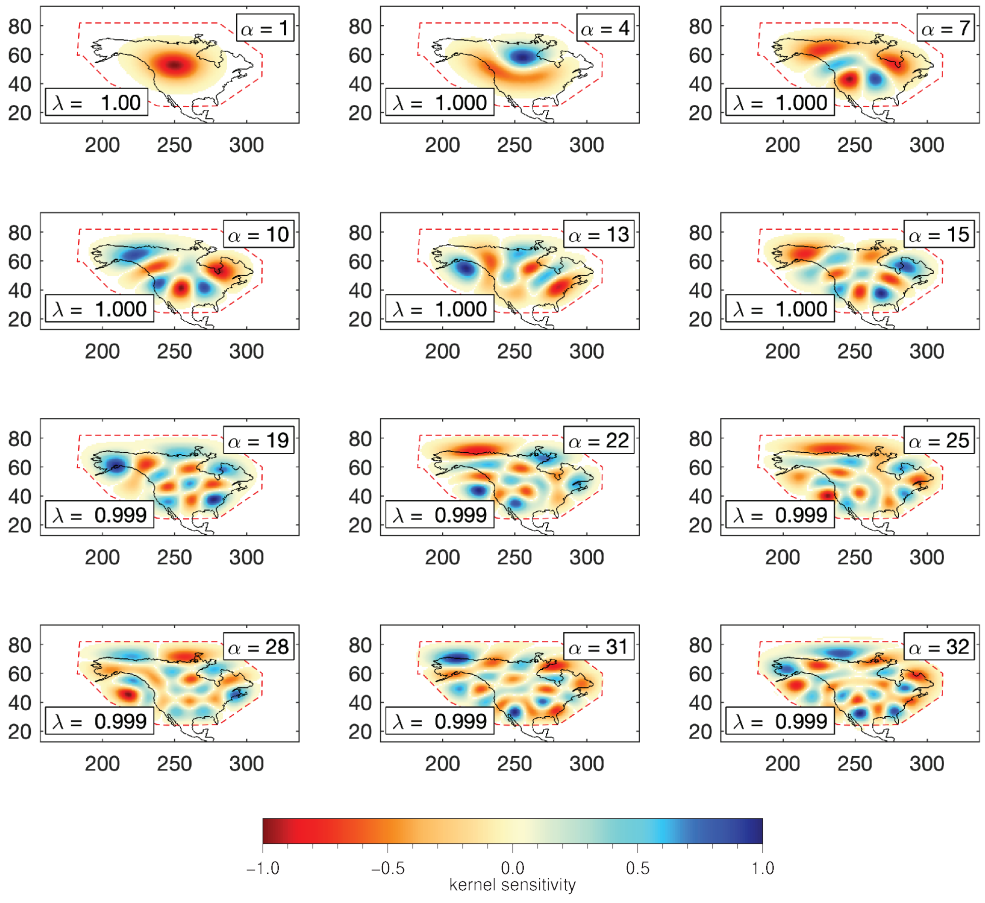

Figure A1. Local sensitivity for North America continental region showing plots of synthesized concentrated Slepian eigenfunctions. α indicates the eigenfunction number and rank while the eigenvalue concentration factors are labeled as λ.

A1

Author contributions. A.O.T. and C.H. designed research, performed research, and wrote the paper.

Competing interests. The contact author has declared that neither they nor their co-authors have any competing interests.

https://doi.org/10.5194/se-2021-151
Preprint. Discussion started: 4 January 2022

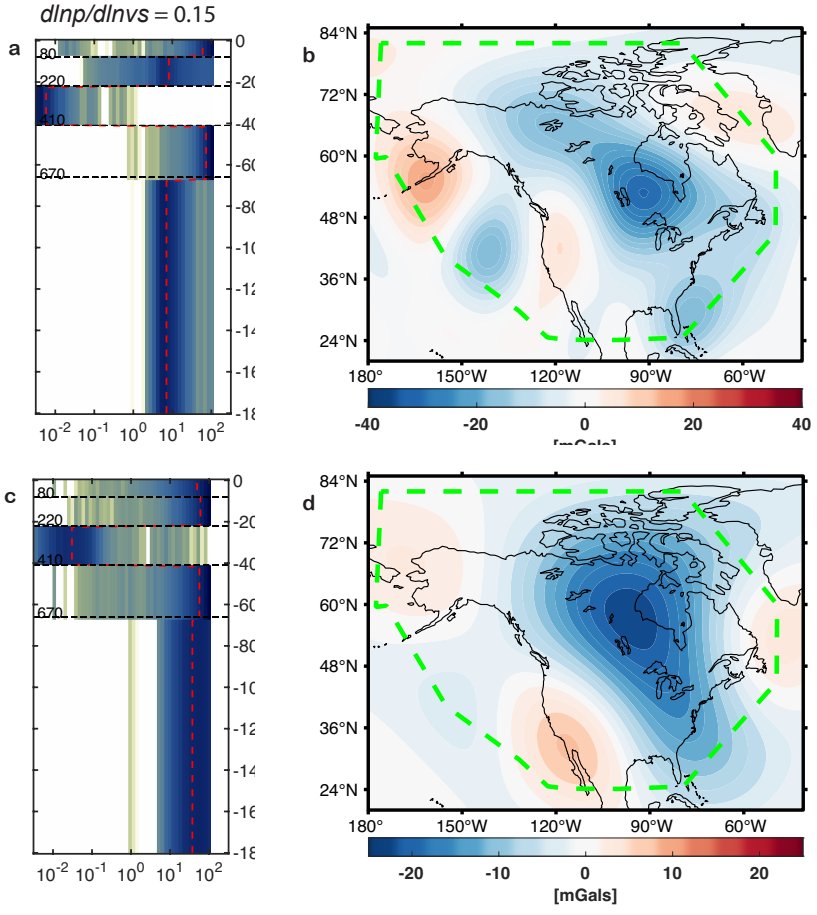

Figure A2. Ensemble of regional relative viscosity solutions of North America continental region for spherical harmonic degree (a) L =2 to 15 and (c) L =2 to 10, based on seismically-derived mantle model from (French and Romanowicz, 2015) using constant seismic velocities to density scaling of 0.15. The dash red lines in each panel shows the average viscosity from each solution. Horizontal dash black lines are our a prior mantle interfaces used in our MCMC inversions. The averages of the resulting modeled free-air gravity field, which are ensemble from the MCMC calculation are shown in **b** for L =2 to 15 and **d** for L =2 to 10.

https://doi.org/10.5194/se-2021-151
Preprint. Discussion started: 4 January 2022

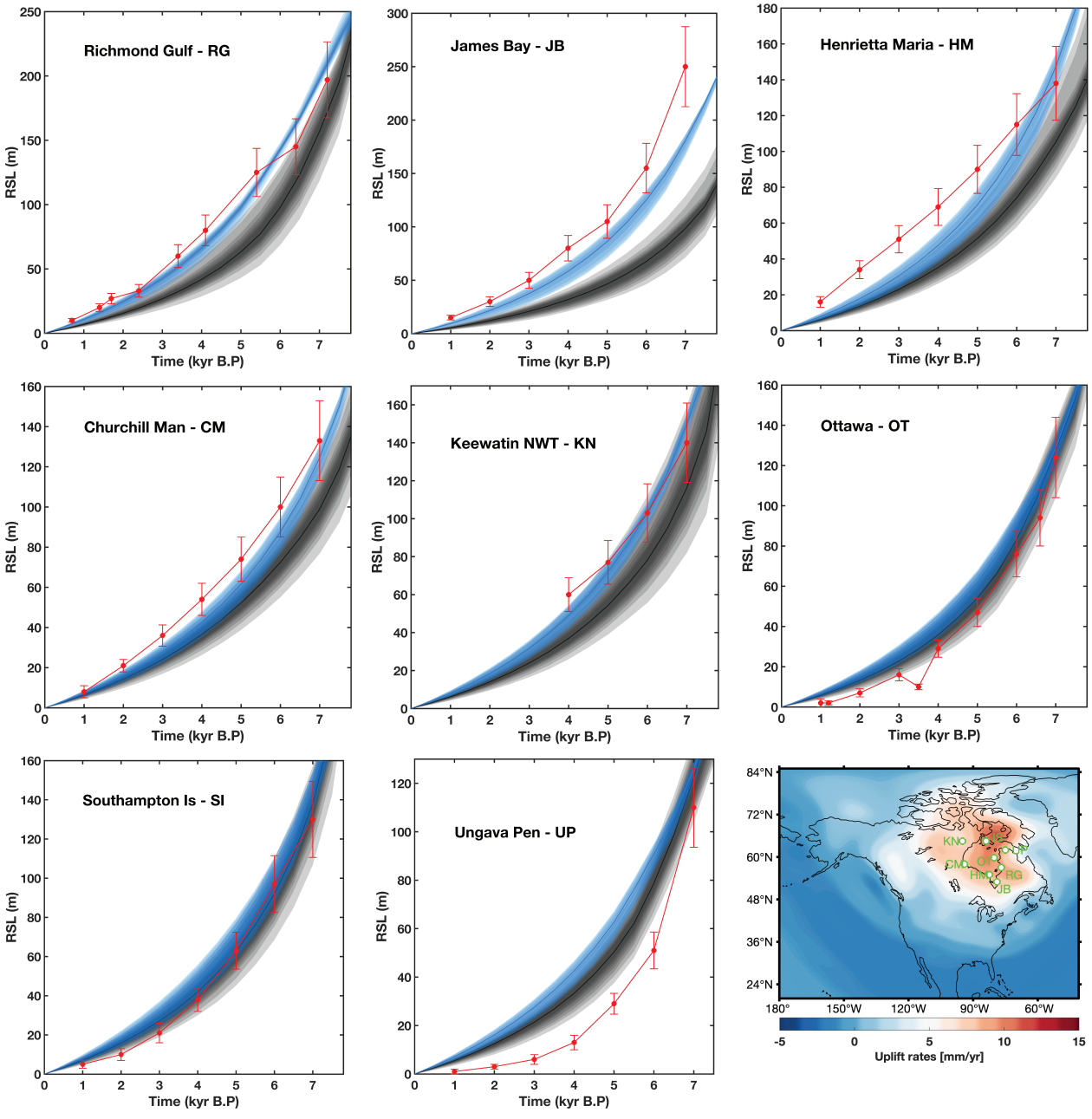

Figure A3. Ensemble RSL predictions from our joint inversion considering the entire NA continental area with a weighting ($\alpha = 2$) applied to the RSL. The blue shades correspond to our viscosity inference with the locally synthesized deglaciation model ICE-6G (Peltier et al., 2015) while the dark shades are based on GLAC1D-NA ice sheet model from Tarasov et al. (2012) for the North America region. The respective red lines with σ error bars are the observed relative sea level for the Hudson Bay. Each panel shows a plot of RSL heights in meters against time in 1000 years. The lower right conner map shows the resulting postglacial average uplift sampled from a few 1000s iterations at the end of the joint inversion with RSL sites name ID in green. The mantle flow component of the joint inversion used the Simmons et al. (2010) seismic conversion profile in both calculations.

https://doi.org/10.5194/se-2021-151
Preprint. Discussion started: 4 January 2022

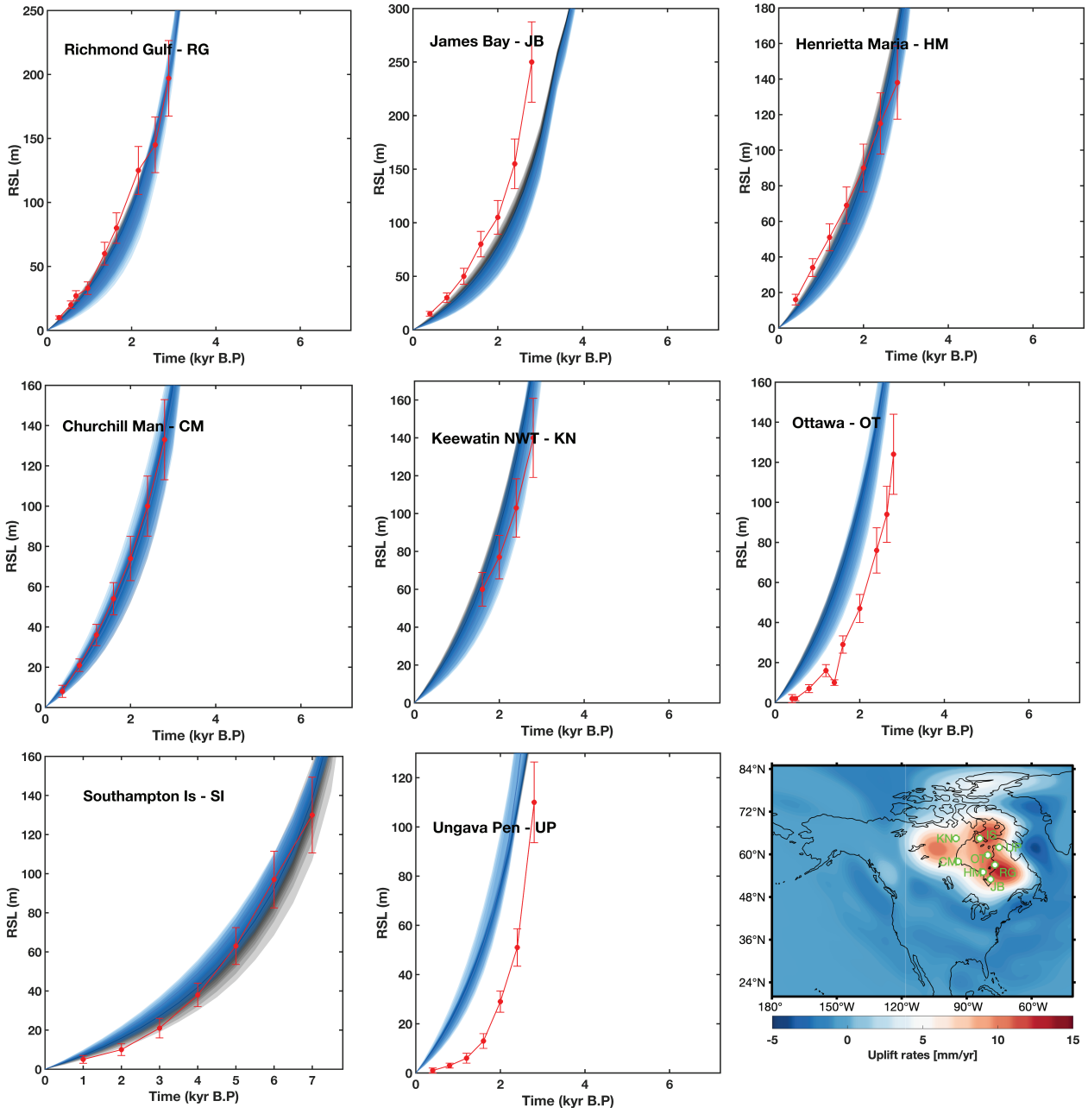

Figure A4. Same as figure A3 with no weighting ($\alpha = 1$) applied but The mantle flow component of the joint inversion uses constant seismic conversion parameter of $\delta ln\rho/\delta lnv_S = 0.3$. The lower right conner map shows the resulting postglacial average uplift sampled from a few 1000s iterations at the end of the joint inversion and RSL sites name ID given in green.

https://doi.org/10.5194/se-2021-151
Preprint. Discussion started: 4 January 2022

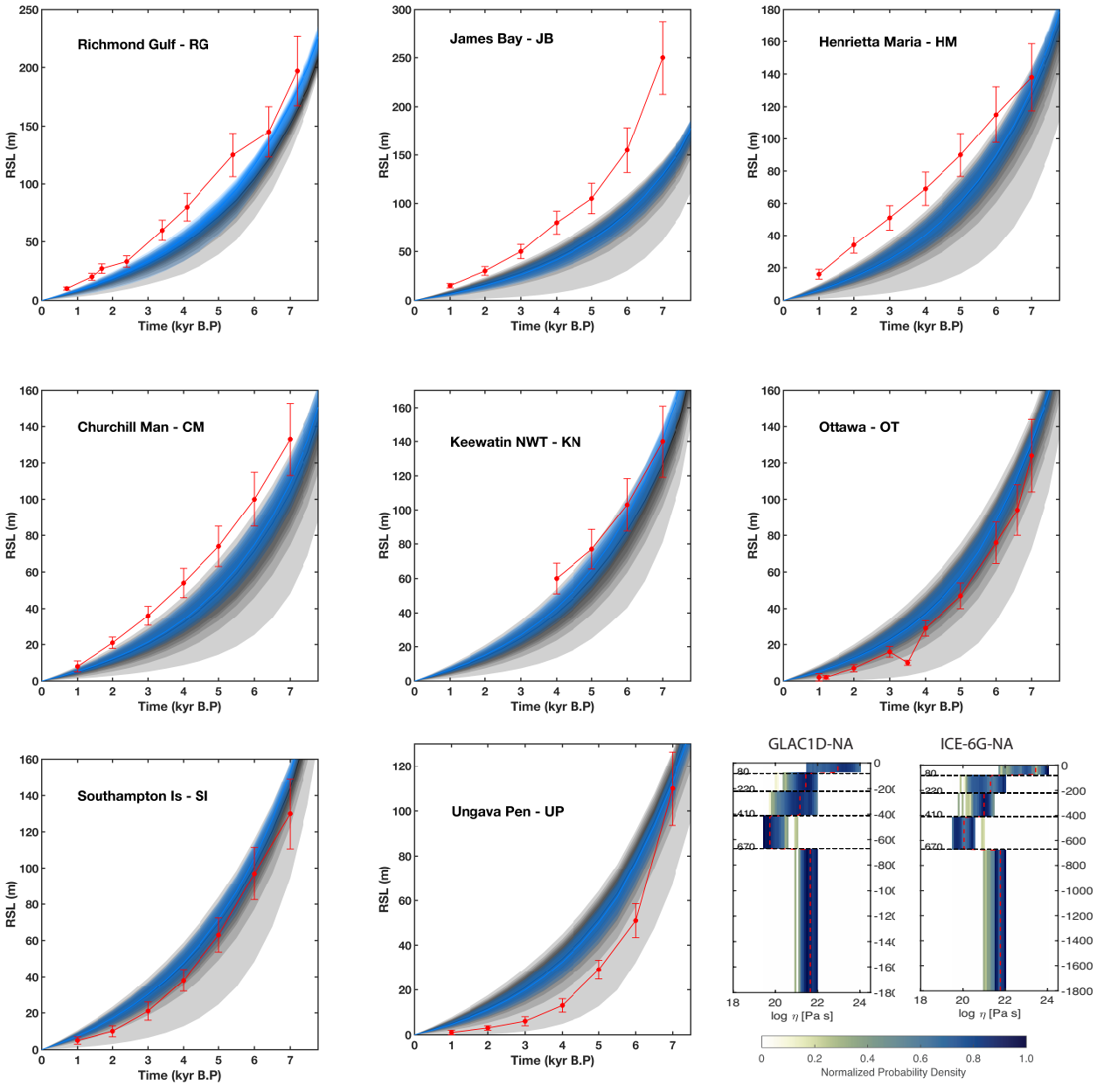

Figure A5. Ensemble RSL predictions from our joint inversion considering the entire NA continental area with L =2 to 10 for local mantle flow model for viscosity inference. The blue shades correspond to our viscosity inference with the locally synthesized deglaciation model ICE-6G (Peltier et al., 2015) while the dark shades are based on GLAC1D-NA ice sheet model from Tarasov et al. (2012) for the North America region. The respective red lines with σ error bars are the observed relative sea level for the Hudson Bay. Each panel shows a plot of RSL heights in meters against time in 1000 years. The lower right conner panels show the resulting ensemble of regional viscosity solutions of North America continental region using the Simmons et al. (2010) seismic conversion profile in each deglaciation model.

https://doi.org/10.5194/se-2021-151
Preprint. Discussion started: 4 January 2022

Acknowledgements. We appreciate the University of Arizona's High Performance Computing center for granting us the computational resources for the study. Figures were created with GMT and Matlab, and the accompanying numerical code for our calculations. **Funding**:This work was made possible by NASA grant NNX17AE18G to CH.

https://doi.org/10.5194/se-2021-151
Preprint. Discussion started: 4 January 2022

References

F. J. Simons A. Plattner. High-resolution local magnetic field models for the martian south pole from mars global surveyor data. *J. Geophys. Res.,*, 120:1543–1566, 2015. https://doi.org/https://doi.org/10.1002/2015JE004869.

Kadircan Aktas and David W. Eaton. Upper-mantle velocity structure of the lower great lakes region. *Tectonophysics*, 420(1):267–281, 2006. ISSN 0040-1951. https://doi.org/https://doi.org/10.1016/j.tecto.2006.01.020. URL https://www.sciencedirect.com/science/article/pii/S0040195106000990. Seismic Probing of Continents and their Margins.

Franz Aurenhammer. Voronoi diagrams - a survey of a fundamental geometric data structure. *ACM Computing Surveys*, 23(3):345–405, 1991. ISSN 0360-0300.

Oliver Baur and Nico Sneeuw. Assessing greenland ice mass loss by means of point-mass modeling: a viable methodology. *Journal of Geodesy*, 85(9):607–615, Sep 2011. ISSN 1432-1394. https://doi.org/10.1007/s00190-011-0463-1. URL https://doi.org/10.1007/s00190-011-0463-1.

Michael Bevis, Christopher Harig, Shfaqat A. Khan, Abel Brown, Frederik J. Simons, Michael Willis, Xavier Fettweis, Michiel R. van den Broeke, Finn Bo Madsen, Eric Kendrick, Dana J. Caccamise, Tonie van Dam, Per Knudsen, and Thomas Nylen. Accelerating changes in ice mass within greenland, and the ice sheet's sensitivity to atmospheric forcing. *Proceedings of the National Academy of Sciences*, 116 (6):1934–1939, 2019. ISSN 0027-8424. https://doi.org/10.1073/pnas.1806562116. URL https://www.pnas.org/content/116/6/1934.

T. Bodin, M. Sambridge, K. Gallagher, and N. Rawlinson. Transdimensional inversion of receiver functions and surface wave dispersion. *Journal of Geophysical Research: Solid Earth*, 117(B2):B02301, 2012. https://doi.org/https://doi.org/10.1029/2011JB008560. URL https://agupubs.onlinelibrary.wiley.com/doi/abs/10.1029/2011JB008560.

Victor E. Camp, Martin E. Ross, Robert A. Duncan, and David L. Kimbrough. Uplift, rupture, and rollback of the farallon slab reflected in volcanic perturbations along the yellowstone adakite hot spot track. *Journal of Geophysical Research: Solid Earth*, 122(9):7009–7041, 2017. https://doi.org/https://doi.org/10.1002/2017JB014517. URL https://agupubs.onlinelibrary.wiley.com/doi/abs/10.1002/2017JB014517.

S. Cianetti, C. Giunchi, and G. Spada. Mantle viscosity beneath the hudson bay: An inversion based on the metropolis algorithm. *Journal of Geophysical Research: Solid Earth*, 107(B12):ETG 12–1–ETG 12–15, 2002. https://doi.org/https://doi.org/10.1029/2001JB000585. URL https://agupubs.onlinelibrary.wiley.com/doi/abs/10.1029/2001JB000585.

Geoffrey F. Davies. Penetration of plates and plumes through the mantle transition zone. *Earth and Planetary Science Letters*, 133(3): 507–516, 1995. ISSN 0012-821X. https://doi.org/https://doi.org/10.1016/0012-821X(95)00039-F. URL https://www.sciencedirect.com/science/article/pii/0012821X9500039F.

Geoffrey F. Davies and Mark A. Richards. Mantle convection. *The Journal of Geology*, 100(2):151–206, 1992. https://doi.org/10.1086/629582. URL https://doi.org/10.1086/629582.

V K Dyke, A S; Prest. *Géographie physique et Quaternaire*, 41:237–263, 1987. ISSN 2. https://doi.org/10.7202/032681ar. URL https://doi.org/10.7202/032681ar.

Adam M. Dziewonski and Don L. Anderson. Preliminary reference earth model. *Physics of the Earth and Planetary Interiors*, 25(4): 297–356, 1981. ISSN 0031-9201. https://doi.org/https://doi.org/10.1016/0031-9201(81)90046-7. URL https://www.sciencedirect.com/science/article/pii/0031920181900467.

W. E. Farrell and J. A. Clark. On postglacial sea level. *Geophysical Journal of the Royal Astronomical Society*, 46(3):647–667, 1976. https://doi.org/https://doi.org/10.1111/j.1365-246X.1976.tb01252.x. URL https://onlinelibrary.wiley.com/doi/abs/10.1111/j.1365-246X.1976.tb01252.x.

https://doi.org/10.5194/se-2021-151
Preprint. Discussion started: 4 January 2022

Alessandro M. Forte and Jerry X. Mitrovica. New inferences of mantle viscosity from joint inversion of long-wavelength mantle convection and post-glacial rebound data. *Geophysical Research Letters*, 23(10):1147–1150, 1996. https://doi.org/https://doi.org/10.1029/96GL00964. URL https://agupubs.onlinelibrary.wiley.com/doi/abs/10.1029/96GL00964.

Alessandro M. Forte and Richard Peltier. Viscous flow models of global geophysical observables: 1. forward problems. *Journal of Geophysical Research: Solid Earth*, 96(B12):20131–20159, 1991. https://doi.org/10.1029/91JB01709. URL https://agupubs.onlinelibrary.wiley.com/doi/abs/10.1029/91JB01709.

A.M. Forte, R. Moucha, N.A. Simmons, S.P. Grand, and J.X. Mitrovica. Deep-mantle contributions to the surface dynamics of the north american continent. *Tectonophysics*, 481(1):3–15, 2010. ISSN 0040-1951. https://doi.org/https://doi.org/10.1016/j.tecto.2009.06.010. URL https://www.sciencedirect.com/science/article/pii/S0040195109003308. Insights into the Earth's Deep Lithosphere.

Scott French and Barbara Romanowicz. Broad plumes rooted at the base of the earth's mantle beneath major hotspots. *Nature*, 525:95, 2015. https://doi.org/https://doi.org/10.1038/nature14876. URL https://www.nature.com/articles/nature14876supplementary-information.

A. Ghosh, T. W. Becker, and S. J. Zhong. Effects of lateral viscosity variations on the geoid. *Geophysical Research Letters*, 37(1), 2010. https://doi.org/10.1029/2009GL040426. URL https://agupubs.onlinelibrary.wiley.com/doi/abs/10.1029/2009GL040426.

Peter J. Green. Reversible jump Markov chain Monte Carlo computation and Bayesian model determination. *Biometrika*, 82(4):711–732, 1995. ISSN 0006-3444. https://doi.org/10.1093/biomet/82.4.711. URL https://doi.org/10.1093/biomet/82.4.711.

B. H. Hager and M. A. Richards. Long-wavelength variations in earth's geoid: Physical models and dynamical implications. *Philosophical Transactions of the Royal Society of London. Series A, Mathematical and Physical Sciences*, 328(1599):309–327, 1989. ISSN 00804614.

Bradford H. Hager and Robert W. Clayton. Constraints on the structure of mantle convection using seismic observations, flow models, and the geoid. *Gordon and Breach Science Publishers*, (34637):657–763, 1989. URL http://resolver.caltech.edu/CaltechAUTHORS:20121002-141328164.

Bradford H. Hager, Robert W. Clayton, Mark A. Richards, Robert P. Comer, and Adam M. Dziewonski. Lower mantle heterogeneity, dynamic topography and the geoid. *Nature*, 313(6003):541–545, 1985. https://doi.org/10.1038/313541a0. URL https://doi.org/10.1038/313541a0.

Shin-Chan Han and Frederik J. Simons. Spatiospectral localization of global geopotential fields from the gravity recovery and climate experiment (grace) reveals the coseismic gravity change owing to the 2004 sumatra-andaman earthquake. *Journal of Geophysical Research: Solid Earth*, 113(B1), 2008. https://doi.org/10.1029/2007JB004927. URL https://agupubs.onlinelibrary.wiley.com/doi/abs/10.1029/2007JB004927.

Christopher Harig and Frederik J. Simons. Mapping greenland's mass loss in space and time. *Proceedings of the National Academy of Sciences*, 109(49):19934–19937, 2012. ISSN 0027-8424. https://doi.org/10.1073/pnas.1206785109. URL https://www.pnas.org/content/109/49/19934.

Christopher Harig and Frederik J. Simons. Accelerated west antarctic ice mass loss continues to outpace east antarctic gains. *Earth and Planetary Science Letters*, 415:134–141, 2015. ISSN 0012-821X. https://doi.org/https://doi.org/10.1016/j.epsl.2015.01.029. URL https://www.sciencedirect.com/science/article/pii/S0012821X15000564.

Christopher Harig and Frederik J. Simons. Ice mass loss in greenland, the gulf of alaska, and the canadian archipelago: Seasonal cycles and decadal trends. *Geophysical Research Letters*, 43(7):3150–3159, 2016. https://doi.org/https://doi.org/10.1002/2016GL067759. URL https://agupubs.onlinelibrary.wiley.com/doi/abs/10.1002/2016GL067759.

R. Hartmann, J. Ebbing, and C.P. Conrad. A multiple 1d earth approach (m1dea) to account for lateral viscosity variations in solutions of the sea level equation: An application for glacial isostatic adjustment by antarctic deglaciation. *Journal of Geodynamics*, 135:101695,

https://doi.org/10.5194/se-2021-151
Preprint. Discussion started: 4 January 2022

2020. ISSN 0264-3707. https://doi.org/https://doi.org/10.1016/j.jog.2020.101695. URL https://www.sciencedirect.com/science/article/pii/S0264370719301802.

N. A. Haskell. The motion of a viscous fluid under a surface load. *Physics*, 6(8):265–269, 1935. https://doi.org/10.1063/1.1745329. URL https://doi.org/10.1063/1.1745329.

R.D. Hyndman. Lower-crustal flow and detachment in the North American Cordillera: a consequence of Cordillera-wide high temperatures. *Geophysical Journal International*, 209(3):1779–1799, 04 2017. ISSN 0956-540X. https://doi.org/10.1093/gji/ggx138. URL https://doi.org/10.1093/gji/ggx138.

Thomas James, Evan J. Gowan, Ian Hutchinson, John J. Clague, J. Vaughn Barrie, and Kim W. Conway. Sea-level change and paleogeographic reconstructions, southern vancouver island, british columbia, canada. *Quaternary Science Reviews*, 28(13):1200–1216, 2009a. ISSN 0277-3791. https://doi.org/https://doi.org/10.1016/j.quascirev.2008.12.022.

Thomas S. James, John J. Clague, Kelin Wang, and Ian Hutchinson. Postglacial rebound at the northern cascadia subduction zone. *Quaternary Science Reviews*, 19(14):1527–1541, 2000. ISSN 0277-3791. https://doi.org/https://doi.org/10.1016/S0277-3791(00)00076-7.

Thomas S. James, Evan J. Gowan, Ikuko Wada, and Kelin Wang. Viscosity of the asthenosphere from glacial isostatic adjustment and subduction dynamics at the northern cascadia subduction zone, british columbia, canada. *Journal of Geophysical Research: Solid Earth*, 114(B4):B04405, 2009b. https://doi.org/https://doi.org/10.1029/2008JB006077.

Thomas H. Jordan. Structure and formation of the continental tectosphere. *Journal of Petrology*, Special Volume(1):11–37, 01 1988. ISSN 0022-3530. https://doi.org/10.1093/petrology/Special Volume.1.11.

Shun-ichiro Karato and Patrick Wu. Rheology of the upper mantle: A synthesis. *Science*, 260(5109):771–778, 1993. https://doi.org/10.1126/science.260.5109.771. URL https://science.sciencemag.org/content/260/5109/771.

Georg Kaufmann and Kurt Lambeck. Glacial isostatic adjustment and the radial viscosity profile from inverse modeling. *Journal of Geophysical Research: Solid Earth*, 107(B11):ETG 5–1–ETG 5–15, 2002. https://doi.org/https://doi.org/10.1029/2001JB000941. URL https://agupubs.onlinelibrary.wiley.com/doi/abs/10.1029/2001JB000941.

Shfaqat A. Khan, Ingo Sasgen, Michael Bevis, Tonie van Dam, Jonathan L. Bamber, John Wahr, Michael Willis, Kurt H. Kjær, Bert Wouters, Veit Helm, Beata Csatho, Kevin Fleming, Anders A. Bjørk, Andy Aschwanden, Per Knudsen, and Peter Kuipers Munneke. Geodetic measurements reveal similarities between post–last glacial maximum and present-day mass loss from the greenland ice sheet. *Science Advances*, 2(9), 2016. https://doi.org/10.1126/sciadv.1600931.

Scott D. King. An evolving view of transition zone and midmantle viscosity. *Geochemistry, Geophysics, Geosystems*, 17(3):1234–1237, 2016. https://doi.org/https://doi.org/10.1002/2016GC006279.

Scott D. King and Guy Masters. An inversion for radial viscosity structure using seismic tomography. *Geophysical Research Letters*, 19(15):1551–1554, 1992. https://doi.org/https://doi.org/10.1029/92GL01700. URL https://agupubs.onlinelibrary.wiley.com/doi/abs/10.1029/92GL01700.

Corné Kreemer, William C. Hammond, and Geoffrey Blewitt. A robust estimation of the 3-d intraplate deformation of the north american plate from gps. *Journal of Geophysical Research: Solid Earth*, 123(5):4388–4412, 2018. https://doi.org/https://doi.org/10.1029/2017JB015257. URL https://agupubs.onlinelibrary.wiley.com/doi/abs/10.1029/2017JB015257.

Kurt Lambeck, Catherine Smither, and Paul Johnston. Sea-level change, glacial rebound and mantle viscosity for northern Europe. *Geophysical Journal International*, 134(1):102–144, 07 1998. ISSN 0956-540X. https://doi.org/10.1046/j.1365-246x.1998.00541.x. URL https://doi.org/10.1046/j.1365-246x.1998.00541.x.

https://doi.org/10.5194/se-2021-151
Preprint. Discussion started: 4 January 2022

585 Harriet C. P. Lau, Jerry X. Mitrovica, Jacqueline Austermann, Ophelia Crawford, David Al-Attar, and Konstantin Latychev. Inferences of mantle viscosity based on ice age data sets: Radial structure. *Journal of Geophysical Research: Solid Earth*, 121(10):6991–7012, 2016. https://doi.org/https://doi.org/10.1002/2016JB013043. URL https://agupubs.onlinelibrary.wiley.com/doi/abs/10.1002/2016JB013043.

Xi Liu and Shijie Zhong. Constraining mantle viscosity structure for a thermochemical mantle using the geoid observation. *Geochemistry, Geophysics, Geosystems*, 17(3):895–913, 2016. https://doi.org/10.1002/2015GC006161. URL https://agupubs.onlinelibrary.wiley.com/
590 doi/abs/10.1002/2015GC006161.

J. X. Mitrovica and W. R. Peltier. On postglacial geoid subsidence over the equatorial oceans. *Journal of Geophysical Research: Solid Earth*, 96(B12):20053–20071, 1991. https://doi.org/10.1029/91JB01284. URL https://agupubs.onlinelibrary.wiley.com/doi/abs/10.1029/91JB01284.

J. X. Mitrovica and W. R. Peltier. Constraints on mantle viscosity based upon the inversion of post-glacial uplift data from the Hud-
595 son Bay region. *Geophysical Journal International*, 122(2):353–377, 09 1995. ISSN 0956-540X. https://doi.org/10.1111/j.1365-246X.1995.tb07002.x. URL https://doi.org/10.1111/j.1365-246X.1995.tb07002.x.

J. X. Mitrovica, J. L. Davis, and I. I. Shapiro. A spectral formalism for computing three-dimensional deformations due to surface loads: 2. present-day glacial isostatic adjustment. *Journal of Geophysical Research: Solid Earth*, 99(B4):7075–7101, 1994. https://doi.org/https://doi.org/10.1029/93JB03401. URL https://agupubs.onlinelibrary.wiley.com/doi/abs/10.1029/93JB03401.

600 Jerry X. Mitrovica. Haskell [1935] revisited. *Journal of Geophysical Research: Solid Earth*, 101(B1):555–569, 1996. https://doi.org/https://doi.org/10.1029/95JB03208. URL https://agupubs.onlinelibrary.wiley.com/doi/abs/10.1029/95JB03208.

Jerry X. Mitrovica and Alessandro M. Forte. Radial profile of mantle viscosity: Results from the joint inversion of convection and postglacial rebound observables. *Journal of Geophysical Research: Solid Earth*, 102(B2):2751–2769, 1997. https://doi.org/10.1029/96JB03175. URL https://agupubs.onlinelibrary.wiley.com/doi/abs/10.1029/96JB03175.

605 Jerry X. Mitrovica and Glenn A. Milne. On post-glacial sea level: I. General theory. *Geophysical Journal International*, 154(2):253–267, 08 2003. ISSN 0956-540X. https://doi.org/10.1046/j.1365-246X.2003.01942.x. URL https://doi.org/10.1046/j.1365-246X.2003.01942.x.

Jerry X. Mitrovica, Carling C. Hay, Eric Morrow, Robert E. Kopp, Mathieu Dumberry, and Sabine Stanley. Reconciling past changes in earth's rotation with 20th century global sea-level rise: Resolving munk's enigma. *Science Advances*, 1(11), 2015. https://doi.org/10.1126/sciadv.1500679. URL https://advances.sciencemag.org/content/1/11/e1500679.

610 J.X. Mitrovica and A.M. Forte. A new inference of mantle viscosity based upon joint inversion of convection and glacial isostatic adjustment data. *Earth and Planetary Science Letters*, 225(1):177 – 189, 2004. ISSN 0012-821X. https://doi.org/https://doi.org/10.1016/j.epsl.2004.06.005. URL http://www.sciencedirect.com/science/article/pii/S0012821X04003747.

Masao Nakada and Kurt Lambeck. Late Pleistocene and Holocene sea-level change in the Australian region and mantle rheology. *Geophysical Journal International*, 96(3):497–517, 03 1989. ISSN 0956-540X. https://doi.org/10.1111/j.1365-246X.1989.tb06010.x. URL
615 https://doi.org/10.1111/j.1365-246X.1989.tb06010.x.

Eiji Ohtani, Liang Yuan, Itaru Ohira, Anton Shatskiy, and Konstantin Litasov. Fate of water transported into the deep mantle by slab subduction. *Journal of Asian Earth Sciences*, 167:2–10, 2018. ISSN 1367-9120. https://doi.org/https://doi.org/10.1016/j.jseaes.2018.04.024. URL https://www.sciencedirect.com/science/article/pii/S1367912018301469. Asian Orogeny and Continental Tectonics from Geochemical Perspectives, A Special Issue in Memory of Professor Bor-ming Jahn for His Scientific Contributions and Service (Part II).

620 Giovanni Pari and W. Richard Peltier. The free-air gravity constraint on subcontinental mantle dynamics. *Journal of Geophysical Research: Solid Earth*, 101(B12):28105–28132, 1996. https://doi.org/https://doi.org/10.1029/96JB02099. URL https://agupubs.onlinelibrary.wiley.com/doi/abs/10.1029/96JB02099.

https://doi.org/10.5194/se-2021-151
Preprint. Discussion started: 4 January 2022

Giovanni Pari and W. Richard Peltier. Subcontinental mantle dynamics: A further analysis based on the joint constraints of dynamic surface topography and free-air graviy. *Journal of Geophysical Research: Solid Earth*, 105(B3):5635–5662, 2000. https://doi.org/https://doi.org/10.1029/1999JB900349. URL https://agupubs.onlinelibrary.wiley.com/doi/abs/10.1029/1999JB900349.

Archie Paulson and Mark A. Richards. On the resolution of radial viscosity structure in modelling long-wavelength postglacial rebound data. *Geophysical Journal International*, 179(3):1516–1526, 12 2009. ISSN 0956-540X. https://doi.org/10.1111/j.1365-246X.2009.04362.x. URL https://doi.org/10.1111/j.1365-246X.2009.04362.x.

Archie Paulson, Shijie Zhong, and John Wahr. Limitations on the inversion for mantle viscosity from postglacial rebound. *Geophysical Journal International*, 168(3):1195–1209, 03 2007. ISSN 0956-540X. https://doi.org/10.1111/j.1365-246X.2006.03222.x. URL https://doi.org/10.1111/j.1365-246X.2006.03222.x.

W. R. Peltier, D. F. Argus, and R. Drummond. Space geodesy constrains ice age terminal deglaciation: The global ice-6g_c (vm5a) model. *Journal of Geophysical Research: Solid Earth*, 120(1):450–487, 2015. https://doi.org/https://doi.org/10.1002/2014JB011176. URL https://agupubs.onlinelibrary.wiley.com/doi/abs/10.1002/2014JB011176.

Christoph Reigber, Roland Schmidt, Frank Flechtner, Rolf König, Ulrich Meyer, Karl-Hans Neumayer, Peter Schwintzer, and Sheng Yuan Zhu. An earth gravity field model complete to degree and order 150 from grace: Eigen-grace02s. *Journal of Geodynamics*, 39(1):1 – 10, 2005. ISSN 0264-3707. https://doi.org/https://doi.org/10.1016/j.jog.2004.07.001. URL http://www.sciencedirect.com/science/article/pii/S0264370704000754.

J. M. Reusen, B. C. Root, W. Szwillus, J. Fullea, and W. van der Wal. Long-wavelength gravity field constraint on the lower mantle viscosity in north america. *Journal of Geophysical Research: Solid Earth*, 125(12):e2020JB020484, 2020. https://doi.org/https://doi.org/10.1029/2020JB020484. URL https://agupubs.onlinelibrary.wiley.com/doi/abs/10.1029/2020JB020484.

Mark A. Richards and Bradford H. Hager. Geoid anomalies in a dynamic earth. *Journal of Geophysical Research: Solid Earth*, 89(B7):5987–6002, 1984. https://doi.org/10.1029/JB089iB07p05987. URL https://agupubs.onlinelibrary.wiley.com/doi/abs/10.1029/JB089iB07p05987.

Keven Roy and W.R. Peltier. Glacial isostatic adjustment, relative sea level history and mantle viscosity: reconciling relative sea level model predictions for the U.S. East coast with geological constraints. *Geophysical Journal International*, 201(2):1156–1181, 03 2015. ISSN 0956-540X. https://doi.org/10.1093/gji/ggv066. URL https://doi.org/10.1093/gji/ggv066.

Maxwell L. Rudolph, Vedran Lekić, and Carolina Lithgow-Bertelloni. Viscosity jump in earth's mid-mantle. *Science*, 350(6266):1349–1352, 2015. ISSN 0036-8075. https://doi.org/10.1126/science.aad1929. URL http://science.sciencemag.org/content/350/6266/1349.

Maxwell L. Rudolph, Diogo L. Lourenço, Pritwiraj Moulik, and Vedran Lekić. *Long-Wavelength Mantle Structure*, chapter 1, pages 1–19. American Geophysical Union (AGU), 2021. ISBN 9781119528609. https://doi.org/https://doi.org/10.1002/9781119528609.ch1. URL https://agupubs.onlinelibrary.wiley.com/doi/abs/10.1002/9781119528609.ch1.

M. Sambridge, T. Bodin, K. Gallagher, and H. Tkalčić. Transdimensional inference in the geosciences. *Philosophical Transactions of the Royal Society A: Mathematical, Physical and Engineering Sciences*, 371(1984):20110547, 2013. https://doi.org/10.1098/rsta.2011.0547. URL https://royalsocietypublishing.org/doi/abs/10.1098/rsta.2011.0547.

Michael Schmidt, Martin Fengler, Torsten Mayer-Gürr, Annette Eicker, Jürgen Kusche, Laura Sánchez, and Shin-Chan Han. Regional gravity modeling in terms of spherical base functions. *Journal of Geodesy*, 81(1):17–38, Jan 2007. ISSN 1432-1394. https://doi.org/10.1007/s00190-006-0101-5. URL https://doi.org/10.1007/s00190-006-0101-5.

https://doi.org/10.5194/se-2021-151
Preprint. Discussion started: 4 January 2022

Nathan A. Simmons, Alessandro M. Forte, Lapo Boschi, and Stephen P. Grand. Gypsum: A joint tomographic model of mantle density and seismic wave speeds. *Journal of Geophysical Research: Solid Earth*, 115(B12), 2010. https://doi.org/10.1029/2010JB007631. URL https://agupubs.onlinelibrary.wiley.com/doi/abs/10.1029/2010JB007631.

Frederik J. Simons. Slepian functions and their use in signal estimation and spectral analysis, 2009.

Frederik J. Simons, F. A. Dahlen, and Mark A. Wieczorek. Spatiospectral concentration on a sphere. *SIAM Review*, 48(3):504–536, 2006. https://doi.org/10.1137/S0036144504445765. URL https://doi.org/10.1137/S0036144504445765.

Mark Simons and Bradford H. Hager. Localization of the gravity field and the signature of glacial rebound. *Nature*, 390(6659):500–504, 1997. https://doi.org/10.1038/37339. URL https://doi.org/10.1038/37339.

G. Spada and D. Melini. Selen^4 (selen version 4.0): a fortran program for solving the gravitationally and topographically self-consistent sea-level equation in glacial isostatic adjustment modeling. *Geoscientific Model Development*, 12(12):5055–5075, 2019. https://doi.org/10.5194/gmd-12-5055-2019. URL https://gmd.copernicus.org/articles/12/5055/2019/.

G. Spada, V. R. Barletta, V. Klemann, R. E. M. Riva, Z. Martinec, P. Gasperini, B. Lund, D. Wolf, L. L. A. Vermeersen, and M. A. King. A benchmark study for glacial isostatic adjustment codes. *Geophysical Journal International*, 185(1):106–132, 2011. https://doi.org/https://doi.org/10.1111/j.1365-246X.2011.04952.x. URL https://onlinelibrary.wiley.com/doi/abs/10.1111/j.1365-246X.2011.04952.x.

Bernhard Steinberger and Arthur R. Calderwood. Models of large-scale viscous flow in the Earth's mantle with constraints from mineral physics and surface observations. *Geophysical Journal International*, 167(3):1461–1481, 2006. ISSN 0956-540X. https://doi.org/10.1111/j.1365-246X.2006.03131.x. URL https://doi.org/10.1111/j.1365-246X.2006.03131.x.

M. E. Tamisiea, J. X. Mitrovica, and J. L. Davis. Grace gravity data constrain ancient ice geometries and continental dynamics over laurentia. *Science*, 316(5826):881–883, 2007. ISSN 0036-8075. https://doi.org/10.1126/science.1137157. URL https://science.sciencemag.org/content/316/5826/881.

Albert Tarantola and Bernard Valette. Inverse problems - quest for information. *Journal of Geophysics*, pages 159–170, 1982.

Lev Tarasov, Arthur S. Dyke, Radford M. Neal, and W.R. Peltier. A data-calibrated distribution of deglacial chronologies for the north american ice complex from glaciological modeling. *Earth and Planetary Science Letters*, 315-316:30–40, 2012. ISSN 0012-821X. https://doi.org/https://doi.org/10.1016/j.epsl.2011.09.010. URL https://www.sciencedirect.com/science/article/pii/S0012821X11005243. Sea Level and Ice Sheet Evolution: A PALSEA Special Edition.

A. M. Tushingham and W. R. Peltier. Ice-3g: A new global model of late pleistocene deglaciation based upon geophysical predictions of post-glacial relative sea level change. *Journal of Geophysical Research: Solid Earth*, 96(B3):4497–4523, 1991. https://doi.org/https://doi.org/10.1029/90JB01583. URL https://agupubs.onlinelibrary.wiley.com/doi/abs/10.1029/90JB01583.

O. Čadek and L. Fleitout. Effect of lateral viscosity variations in the core-mantle boundary region on predictions of the long-wavelength geoid. *Studia Geophysica et Geodaetica*, 50(2):217–232, 2006. ISSN 1573-1626. https://doi.org/10.1007/s11200-006-0013-0. URL https://doi.org/10.1007/s11200-006-0013-0.

Karin Wieczerkowski, Jerry X. Mitrovica, and Detlef Wolf. A revised relaxation-time spectrum for Fennoscandia. *Geophysical Journal International*, 139(1):69–86, 10 1999. ISSN 0956-540X. https://doi.org/10.1046/j.1365-246X.1999.00924.x. URL https://doi.org/10.1046/j.1365-246X.1999.00924.x.

Mark A. Wieczorek and Frederik J. Simons. Localized spectral analysis on the sphere. *Geophysical Journal International*, 162(3):655–675, 09 2005. ISSN 0956-540X. https://doi.org/10.1111/j.1365-246X.2005.02687.x. URL https://doi.org/10.1111/j.1365-246X.2005.02687.x.

https://doi.org/10.5194/se-2021-151
Preprint. Discussion started: 4 January 2022

Patrick Wu and W. R. Peltier. Viscous gravitational relaxation. *Geophysical Journal International*, 70(2):435–485, 08 1982. ISSN 0956-540X. https://doi.org/10.1111/j.1365-246X.1982.tb04976.x. URL https://doi.org/10.1111/j.1365-246X.1982.tb04976.x.

Patrick Wu and W. R. Peltier. Glacial isostatic adjustment and the free air gravity anomaly as a constraint on deep mantle viscosity. *Geophysical Journal of the Royal Astronomical Society*, 74(2):377–449, 1983. https://doi.org/https://doi.org/10.1111/j.1365-246X.1983.tb01884.x. URL https://onlinelibrary.wiley.com/doi/abs/10.1111/j.1365-246X.1983.tb01884.x.

Maryam Yousefi, Glenn A. Milne, Ryan Love, and Lev Tarasov. Glacial isostatic adjustment along the pacific coast of central north america. *Quaternary Science Reviews*, 193:288–311, 2018. ISSN 0277-3791. https://doi.org/https://doi.org/10.1016/j.quascirev.2018.06.017.

Maryam Yousefi, Glenn A Milne, and Konstantin Latychev. Glacial isostatic adjustment of the pacific coast of North America: The Influence of lateral earth structure. *Geophysical Journal International*, 02 2021. ISSN 0956-540X. https://doi.org/10.1093/gji/ggab053. URL https://doi.org/10.1093/gji/ggab053.

Huaiyu Yuan and Barbara Romanowicz. Lithospheric layering in the north american craton. *Nature*, 466:1063 – 1068, 2010. ISSN 1476-4687. https://doi.org/10.1038/nature09332. URL https://doi.org/10.1038/nature09332.